Bulletin of Volcanology (2025) 87:31
https://doi.org/10.1007/s00445-025-01813-4

RESEARCH ARTICLE

A late Pleistocene-Holocene record of explosive eruptions from central Sumatra (Indonesia) in the western Sunda volcanic arc

Marcus Phua[1,3] · Francesca Forni[2,3] · Steffen Eisele[3] · Hamdi Rifai[4] · Mahyar Mohtadi[5] · Andreas Lückge[6] · Caroline Bouvet de Maisonneuve[3]

Received: 27 August 2024 / Accepted: 7 March 2025

Abstract

The island of Sumatra within the Indonesian archipelago is home to over 130 active or potentially active volcanoes with a history of explosive eruptions. Highly explosive eruptions with volcanic explosivity index (VEI) ≥ 6 in Sumatra, such as those originating from the massive Toba caldera, have been well-documented in the literature. However, moderately explosive eruptions with VEI 3–5 have received inadequate attention due to their limited preservation within the proximal stratigraphic record. This gap in knowledge hinders existing attempts to conduct hazard assessments for these potentially impactful eruptions. In this study, we address this knowledge gap by presenting a combination of geochemical, geochronological and tephrochronological datasets associated with distal tephra layers sampled from deep-sea cores collected off the coast of West Sumatra, as well as proximal pyroclastic deposits throughout central Sumatra. Our datasets reveal geochemical and stratigraphic correlations between seven distal tephra layers and their proximal sources, allowing for the quantification of their eruption ages and volumes. Notably, we identified the ~ 1.53 ka Lubuk King Tephra (LKT) eruption from Malintang volcano that discharged ≥ 1.4 km^3 dense-rock equivalent (DRE) of magma, representing the youngest known VEI 5 eruption in Sumatra. In addition, we determined Tandikat volcano as the proximal source for a pair of temporally proximate (~ 580 yr apart) VEI 5 eruptions (Tandikat II and I Tephra, TDK II and I; ~ 4.36 and ~ 4.94 ka) that produced ≥ 1.1 and ≥ 2.7 km^3 DRE of magma, respectively. We also ascertained that at least two VEI 4 eruptions occurring within the last ~ 36 kyr can be correlated to the active Marapi volcano. Furthermore, we traced distal tephra layers AB4 (~ 36.8 ka) and AB5 (~ 41.0 ka) to two distinct VEI ≥ 5 eruptions at volcanic centres in neighbouring provinces (Ranau Tuff, RAN from South Sumatra; Djudjun Tephra, DJT from Jambi). Volcanic source provenances for another six distal tephra layers remain unknown due to the lack of known proximal correlatives. Overall, our study provides an improved tephrochronological framework for late Pleistocene-Holocene explosive volcanism in central Sumatra that will help refine existing volcanic hazard assessments and enhance the integration of terrestrial and marine palaeoenvironmental archives regionally.

Keywords Deep-sea tephra · Tephrochronology · Tephrostratigraphy · Eruptive history · Distal tephra record · Proximal stratigraphic record

Editorial responsibility: M. Edmonds.

✉ Marcus Phua
mphua@hku.hk

[1] Department of Earth Sciences, The University of Hong Kong, Hong Kong SAR, China

[2] Dipartimento di Scienze della Terra "Ardito Desio", Università degli Studi di Milano, Milan, Italy 20133

[3] Earth Observatory of Singapore and Asian School of the Environment, Nanyang Technological University, Singapore 639798, Singapore

[4] Departemen Fisika, Universitas Negeri Padang, Kota Padang, Sumatera Barat 25131, Indonesia

[5] MARUM – Center for Marine Environmental Sciences, University of Bremen, Bremen 28359, Germany

[6] Bundesanstalt für Geowissenschaften und Rohstoffe (BGR), Hannover, Germany

Published online: 04 April 2025

Introduction

Sumatra represents the western segment of the Sunda volcanic arc that formed due to the northward subduction of the Indo-Australian plate beneath the Sunda plate (Hutching and Mooney 2021). The western Sunda volcanic arc stretches for ~ 1700 km from Pulau Weh in the northwest to Sunda Straits in the southeast and comprises at least 130 active or potentially active volcanoes, corresponding to ~ 18% of volcanoes throughout Southeast Asia (Whelley et al. 2015). According to the classification of Whelley et al. (2015), Sumatra hosts about one-third of the large calderas (diameter ≥ 5 km) and well-plugged stratovolcanoes (crater diameter: 2.5–5 km) in the region. Assuming the size of a caldera or summit crater is proportional to the size of an eruption, it is conceivable that moderately to highly explosive eruptions with a volcanic explosivity index (VEI; Newhall and Self 1982) between 3 and 8 were relatively common in the recent geological past. Correspondingly, the large quantity of tephra layers sampled within deep-sea cores located hundreds to thousands of kilometres from possible sources highlights the probable frequent nature of explosive Sumatran eruptions during the Quaternary (e.g. Ninkovich 1979; Salisbury et al. 2012; Phua 2022; Kutterolf et al. 2023). However, the occurrence of explosive eruptions in Sumatra is poorly documented due to the lack of thorough stratigraphic reconstructions in the proximal record, underlining a significant knowledge gap in our understanding of its eruptive history (Bouvet de Maisonneuve and Bergal-Kuvikas 2020). This lack of documentation is likely to impact greatly on the record of moderately explosive eruptions (VEI 3–5), as they are typically under-represented in the proximal stratigraphic record (Brown et al. 2014) relative to highly explosive eruptions (VEI ≥ 6) such as those associated with Toba (e.g. Chesner et al. 1991; Szymanowski et al. 2023), Singkut (Forni et al. 2024), Maninjau (e.g. Alloway et al. 2004; Suhendro et al. 2022) and Ranau (Bellier et al. 1999; Natawidjaja et al. 2017) calderas. The sudden and violent awakening of Sinabung in 2010 after > 400 years in dormancy (Hendrasto et al. 2012) resulted in heightened awareness around the hazards of Sumatran volcanoes and further underscores the urgency and necessity for new studies aimed at improving the eruptive history of this active, yet poorly studied region. Given the limited preservation of proximal deposits, deep-sea cores represent an essential archive of explosive Sumatran eruptions. The available distal tephra record indicates the youngest explosive eruptions are likely sourced from the central segment of Sumatra (Salisbury et al. 2012). Three tephra layers (V-3, V-4 and V-5) were preserved in cores collected ~ 300 km off the coast of West Sumatra, however, the provenances of these distal tephra are unknown due to a lack of proximal correlatives.

In this study, we combine field observations and geochemical and geochronological data of proximal pyroclastic deposits from West Sumatra and nearby provinces (Jambi and South Sumatra), along with tephrochronological data from deep-sea cores retrieved by research cruise R/V Sonne between 2005 and 2006 during the SO184 (Hebbeln et al. 2006) and SO189-2 (Wiedicke-Hombach et al. 2006) expeditions. We use major and trace element glass compositions to geochemically fingerprint distal tephra layers and correlate them to their likely proximal sources. We also present new eruption ages, volumes and sizes (VEI), as well as estimates of eruption source parameters. These new findings combine to enhance our knowledge of Sumatran eruptions in terms of their frequency and size. Significantly, our study presents an improved late Pleistocene-Holocene tephrochronological framework for explosive volcanism from central Sumatra in the western Sunda volcanic arc.

Volcanological background

West Sumatra, Jambi and South Sumatra are situated in the central to southern segments of Sumatra and host a cluster of volcanic centres that are pertinent to this study (Fig. 1). Most information concerning these volcanic centres is derived from the Global Volcanism Program database (Smithsonian Institution 2024) as dedicated studies are scarce or missing in the literature. A compilation of the calderas and volcanoes from West Sumatra, as well as those of relevance in Jambi and South Sumatra with available information, is summarised in Table 1.

Of particular interest is West Sumatra where little is known about the eruptive history of Malintang, Talakmau-Pasaman and Melintang. The most prominent volcanic feature in the province is the Maninjau caldera that produced a VEI 7 caldera-forming eruption (~ 52 ka; Alloway et al. 2004). The associated pyroclastic density current (PDC) deposits (i.e. Maninjau Tuff, MJT) cover a large expanse of West Sumatra with thicknesses ≥ 100 m in various locations (Pribadi et al. 2007). Marapi and Talang-Pasar Arbaa are the most active stratovolcanoes in West Sumatra that have produced numerous small explosive eruptions (VEI ≤ 2) historically. In comparison, only three small historical eruptions (VEI 1) have been reported for the active Tandikat-Singgalang stratovolcanoes. Additionally, Hosobuchi et al. (2021) and Suhendro (2024) recognised widespread pyroclastic deposits in the valley between Maninjau and Tandikat-Singgalang (i.e. Malalak Tephra, MT) and attributed its source to Tandikat. The MT is described as a pyroclastic succession composed of an initial ash layer (F-0) overlain by five lapilli layers (F-1 to F-5; Suhendro 2024). All six MT units are

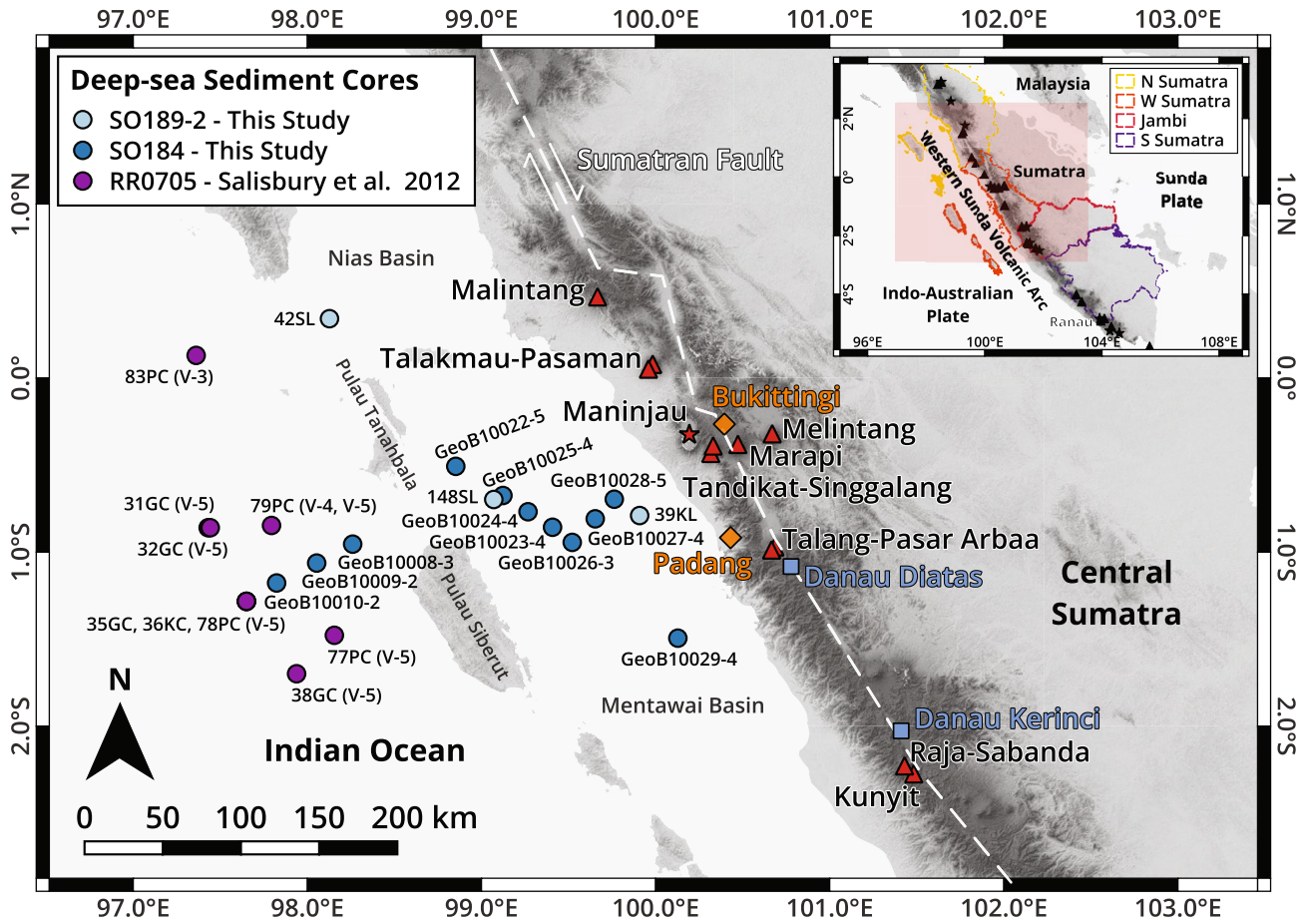

Fig. 1 Geographical map of central Sumatra marked with Quaternary calderas (red stars) and volcanoes (red triangles) of interest in the study. Deep-sea core locations are indicated by light blue circles (cruise SO189-2), blue circles (cruise SO184) and purple circles (cruise RR0705 from Salisbury et al. 2012). Map inset highlights the area covered by the larger map (red shaded box) and the wider Sumatra Island including the provinces of North Sumatra (yellow dash line), West Sumatra (orange dash line), Jambi (red dash line), South Sumatra (purple dash line) and Sumatran calderas (black stars) and volcanoes (black triangles). Hillshade digital elevation model is derived from SRTM 1 Arc-Second Global Dataset (U.S. Geological Survey 2018)

stratigraphically younger than MJT. Apart from the MT, no other deposits of explosive eruptions younger than MJT have been reported in the proximal stratigraphic record. This is contrary to the distal tephra record where evidence for explosive volcanism from central Sumatra is preserved (Salisbury et al. 2012). Tephra layers V-3, V-4 and V-5 of unknown origins were previously identified within deep-sea cores (Salisbury et al. 2012). V-3 is a 1.5 cm-thick andesitic tephra layer found in two cores with a calibrated age of 13,610 ± 315 cal a (1σ), whilst V-4 is a 3.5 cm-thick dacitic ash deposit identified in one core with a calibrated age of 1930 ± 85 cal a (1σ). V-5 is a dacitic to rhyolitic ash layer that occurred within eight cores with thicknesses ranging from 1 to 8 cm and calibrated ages that range between 4690 ± 50 and 4860 ± 30 cal a (1σ). Tandikat has been proposed by Suhendro (2024) as a potential source for V-5 based on similarities in glass compositions with the MT.

Materials and methods

Proximal deposits

The search for proximal deposits in Sumatra is commonly a challenging undertaking. This is due to a combination of the westerly prevailing winds and the perennial high precipitation rates, which result in low preservation potential of volcanic deposits. Furthermore, the dense tropical vegetation cover, as well as intensive and widespread agriculture, impacts greatly on the accessibility and availability of outcrops. In West Sumatra, occurrences of proximal deposits are sparse, except for deposits from the MJT eruption. Despite limited outcrops, tephra fall deposits associated with Malintang, Marapi and Tandikat, as well as a PDC deposit located southeast of Talang, were sampled. Additionally, widely distributed pyroclastic successions sourced from Jambi and South Sumatra were sampled as potential

Table 1 Compilation of information on calderas and volcanoes from West Sumatra, as well as those of relevance to the study in Jambi and South Sumatra

Volcanic centre	Province	Latitude, longitude	Volcano type*	Rock compositions	Description	Eruptive history
Malintang	West Sumatra	0.4667, 99.6666	Semi-plugged stratocone	Basaltic andesite to andesite and dacite	~2-km-wide summit crater breached to the S	*Unknown*
Talakmau-Pasaman	West Sumatra	0.0806, 99.9833	Semi-plugged stratocone	Basaltic andesite to dacite	Twin stratovolcanoes and a parasitic cone	*Unknown*
Maninjau	West Sumatra	−0.3500, 100.2000	Large caldera	Andesite to rhyolite	~20×10 km caldera depression with pre-caldera lavas exposed	~52 ka[a] caldera-forming eruption
Tandikat-Singgalang	West Sumatra	−0.4328, 100.3172	Semi-plugged stratocone	Basaltic andesite to andesite and dacite	~360-m-wide summit crater nested within a partially eroded ~1.2-km-wide caldera	Three historical eruptions (VEI 1) since 1889 CE; Singgalang is extinct
Marapi	West Sumatra	−0.3790, 100.4743	Open-vent stratocone	Andesite to basalt and trachy-andesite	Multiple summit craters within a ~1.4-km-wide caldera	Sixty-eight historical eruptions (VEI 1–2) since 1770 CE
Melintang (or Sago)	West Sumatra	−0.3361, 100.6739	Semi-plugged stratocone	Andesite to basalt	~2-km-wide summit crater breached to the SE	*Unknown*
Talang-Pasar Arbaa	West Sumatra	−0.9789, 100.6811	Open-vent stratocone	Basaltic andesite to andesite	Hydrothermally active summit crater	Thirteen historical eruptions (VEI 1–2) since 1833 CE; Pasar Arbaa is extinct
Raja-Sabanda	Jambi	−2.2256, 101.4275	Semi-plugged stratocone	*Unknown*	~3 km-wide caldera breached to the SE and a parasitic cone to the NE	*Unknown*
Kunyit	Jambi	−2.2694, 101.4858	Semi-plugged stratocone	Dacite	Two hydrothermally active summit craters	*Unknown*
Ranau	South Sumatra	−4.8681, 103.9214	Large caldera	Andesite to rhyolite	~14×8 km caldera depression with pre-caldera lavas exposed and a post-caldera volcano (Seminung)	~34 ka[b] caldera-forming eruption

*Volcano type classification from Whelley et al. (2015); [a]age of Maninjau caldera-forming eruption from Alloway et al. (2004); [b]age of Ranau caldera-forming eruption from Natawidjaja et al. (2017); all other information is from the Global Volcanism Program database (Smithsonian Institution 2024)

Source

correlatives to the distal tephra layers acquired. General descriptions, physical characteristics and sampling locations of the proximal pyroclastic deposits are reported in Table S1 (Online Resource 1).

Distal tephra

Seventeen deep-sea cores collected by R/V Sonne during the SO184 and SO189-2 expeditions were sub-sampled. Fourteen cores from SO184 were sub-sampled at the Center for Marine Environmental Sciences (MARUM) in Bremen, Germany, whereas the remaining three cores from SO189-2 were sub-sampled at the Federal Institute for Geosciences and Natural Resources (BGR) in Hannover, Germany. The locations for these cores form three distinct clusters (Fig. 1): (1) in the northern Mentawai basin, (2) in the central Mentawai basin, and (3) on the accretionary prism southwest of Pulau Tanahbala. The only exception is core 42SL, located in the Nias Basin.

For the description of distal tephra identified in the deep-sea cores, we used the term "ash bed" to define a continuous and discrete ash horizon or ash pod that is predominantly composed of volcanic ash characterised by a generally homogeneous glass composition. Additionally, we utilised the term "ash/tephra layer" to describe multiple ash beds that are correlated between various coring sites, as well as proximal deposits. Secondary (or reworked) ash beds are ascertained based on a combination of characteristics including irregular or disrupted appearances of tephra deposits in which clear indications of bioturbation, mass flows and/or turbidity currents exist, as well as heterogenous glass compositions. General information on the deep-sea cores collected and the physical characteristics of the distal tephra sampled are provided in Table S2 (Online Resource 1).

Geochemistry

Major element glass compositions were analysed with a JEOL JXA-8530F field emission electron probe microanalyser (EPMA) at the Facility for Analysis, Characterisation, Testing and Simulation (FACTS), Nanyang Technological University, Singapore (NTU). Analytical conditions were as follows: 15 kV acceleration voltage, 6 nA beam current and 10 µm size defocused beam. Elements Na, K and Cl were measured first to minimise alkali migration and volatile loss during analysis. Analytical accuracy, precision and instrumental drift were monitored through repeated analysis of secondary standards from INTAV (Kuehn et al. 2011). The EPMA analytical set-up, a complete dataset of major element glass compositions, and analytical accuracy and precision data for the secondary standards, are given in Tables S3-S5 (Online Resource 2).

Trace element glass compositions were measured by laser ablation-inductively coupled plasma-mass spectrometry (LA-ICP-MS) at the Asian School of the Environment (ASE), NTU, using a Teledyne Photon Machines Analyte G2, 193 nm laser ablation system coupled to a single collector Thermo Scientific Element 2 ICP-MS. Analytical conditions were as follows: 15 µm spot size (square), 8-Hz repetition rate, 4 J cm^{-2} laser fluence, and 30-s ablation time. Analytical accuracy, precision, data validation and instrumental drift were monitored via analyses of glass reference standards ATHO-G, BCR-2G and T1-G (Jochum et al. 2005, 2006), as well as secondary standard INTAVC at regular intervals. Data reduction was performed with Iolite 4.0 (Paton et al. 2011) using the trace element data reduction scheme (Woodhead et al. 2007). The LA-ICP-MS analytical set-up, a complete dataset of trace element glass compositions, and analytical accuracy and precision data for the secondary standard are reported in Tables S6-S8 (Online Resource 3).

Geochronology

Eruption ages for proximal deposits and distal tephra were obtained using radiocarbon (^{14}C) dating. Hand-picked planktonic foraminifera were sampled from deep-sea sediment directly below and/or within the tephra to determine maximum age constraints. When this was not possible, the sediment lying above the tephra was also sampled to derive minimum age constraints. Additionally, terrestrial organic material identified at the base of a proximal deposit was sampled to constrain a maximum eruption age. Radiocarbon ages of the foraminifera and organic material were measured using the accelerator mass spectrometry (AMS) technique at the Beta Analytic Testing Laboratory, USA. Conventional radiocarbon ages (^{14}C yr BP) were calibrated with OxCal 4.4 (Bronk Ramsey 2009), using the Marine20 curve (Heaton et al. 2020) for the foraminifera samples, supplemented by a ΔR correction of -117 ± 70 years (Southon et al. 2002) to account for the marine radiocarbon reservoir effect, and the SHCal20 curve (Hogg et al. 2020) for the organic-rich sample. Radiocarbon results were reported as conventional radiocarbon ages—years before present (^{14}C yr BP), as well as calibrated radiocarbon ages—calendar years before present (cal a BP) in the form of median ages, 1 sigma (68.2%) and 2 sigma (95.4%) probability calibrated age ranges. Radiocarbon ages collated from published work (Natawidjaja et al. 2017; Salisbury et al. 2012) were recalibrated using the appropriate curves (i.e. Marine20 and SHCal20) to facilitate unbiased age comparisons. A compilation of the measured and published radiocarbon ages is provided in Table S9 (Online Resource 4).

For ash beds with no direct age constraints due to an absence of foraminifera within sampled sediment intervals,

we utilised a linear interpolation method based upon sediment accumulation rates (SAR) to estimate an eruption age. The SAR is calculated based on the depth and age of a sediment interval (time marker) stratigraphically closest to the ash bed of interest within the same core. This linear interpolation method relies on the assumption that the SAR between the time marker and ash bed within the core remained constant over time. Despite the uncertainties associated with this approach, it provides an estimated eruption age that is relevant for the ash bed, particularly when none is available. In addition, for a correlated ash/tephra layer with multiple radiocarbon ages, we calculated a weighted mean age (and preferred eruption age) using IsoplotR (Vermeesch 2018). The complete dataset of eruption ages determined for the ash beds/layers is given in Table S10 (Online Resource 4).

Tephra correlation

Inter-core and source-to-sink correlations of ash beds/layers were established using information including glass compositions, eruption ages, relative stratigraphic relationships, and textural characteristics. Furthermore, tephra correlation procedures were conducted using a combination of graphical and statistical approaches to compare and match glass compositions, quantify similarity (or dissimilarity) between tephra layers and/or potential sources, and establish the validity of correlations (Lowe et al. 2017). The graphical approach encompasses the use of bivariate plots of elements and elemental ratios to identify inter-core correlations, as well as correlations to likely sources. This is supported by the statistical approach that employs two statistical methods in tandem including the principal component analysis (PCA) and the multi-element hierarchical cluster analysis (MEHCA). The FactoMineR package (Lê et al. 2008) in R was used to perform the PCA and MEHCA analyses. PCA analyses were conducted using multiple glass shard compositions for each ash bed, whilst MEHCA analyses were performed with average glass shard compositions for each ash bed.

Tephra volumes and eruption source parameters

Tephra volumes were estimated for correlated ash/tephra layers and ash beds with a known source. For the ash/tephra layers with sufficient proximal and/or distal thickness data, volumes were obtained by applying the empirical methods of integration including the exponential method of Pyle (1989) modified by Fierstein and Nathenson (1992), as well as the power law (Bonadonna and Houghton 2005) and Weibull methods (Bonadonna and Costa 2012), using the MATLAB package TError (Biass et al. 2014a, 2014b) and the Excel spreadsheets provided by Nathenson and Fierstein (2015) and Bonadonna and Costa (2012). For the ash beds with insufficient distal thickness data, minimum volumes were estimated with the single isopach method of Legros (2000) by assuming an ellipse-shaped isopach with a downwind to crosswind ratio of ~4:1. Eruptions were classified using the VEI scale based on the calculated volumes. The complete isopach dataset, as well as eruption volumes and sizes (VEI) for the ash beds/layers, is reported in Table S11 (Online Resource 5).

Eruption source parameters (ESP) including plume height (*H*), mass eruption rate (*MER*) and duration (*D*) were determined for an eruption with sufficient proximal thickness data and clast diameter measurements, using TError (Biass et al. 2014a, 2014b). Isopleth maps required to characterise these eruptive parameters were compiled by averaging the arithmetic mean of the three main axes for the five largest lithic clasts (Table S12 in Online Resource 5; Biass and Bonadonna 2011). Maximum *H* was estimated by applying the MATLAB implementation of the Carey and Sparks (1986) model developed by Biass et al. (2015), which quantifies *H* for an interpolated range of clast sizes and densities. *MER* was calculated with the empirical methods of Wilson and Walker (1987) and Mastin et al. (2009) that utilises maximum *H* and entrainment constant *k* values of 0.236 and 2, respectively. The method of Degruyter and Bonadonna (2012) was also used to calculate *MER*. Minimum *D* for the eruption was determined using the *MER* and volume. ESP uncertainties were simultaneously assessed using TError. For each reference input parameter, a relative input uncertainty (RIU) is chosen, and then TError runs a Monte Carlo simulation to generate an uncertainty distribution (Gaussian) symmetrically centred around the reference value. Each ESP is subsequently expressed as the median of its distribution. 20% RIU was chosen for each input parameter and 10,000 iterations of Monte Carlo simulation were run for each analysis. The complete dataset of TError input parameters and output ESP is provided in Table S13 (Online Resource 5).

Results

Proximal stratigraphic record

Major and trace element glass chemistry and/or eruption ages were obtained for proximal pyroclastic deposits associated with five volcanic centres in West Sumatra, one in Jambi and one in South Sumatra. Juvenile glass compositions of the proximal deposits predominantly range from dacitic to rhyolitic (Fig. 2a), except for the Marapi deposits, which reflect more diverse and alkali-rich compositions (i.e. trachyandesitic to trachydacitic and high K_2O rhyolitic; Fig. 2a). Overall, the various proximal sources are best discriminated based on the K_2O vs. CaO, La/Th vs. Zr/Y, La/Yb vs. Zr/Nb and Rb/Y vs. Ba/La bivariate plots (Fig. 3; Figs. S1 and S2 in Online Resource 6). The representative juvenile glass compositions for the proximal pyroclastic deposits are summarised in Table 2.

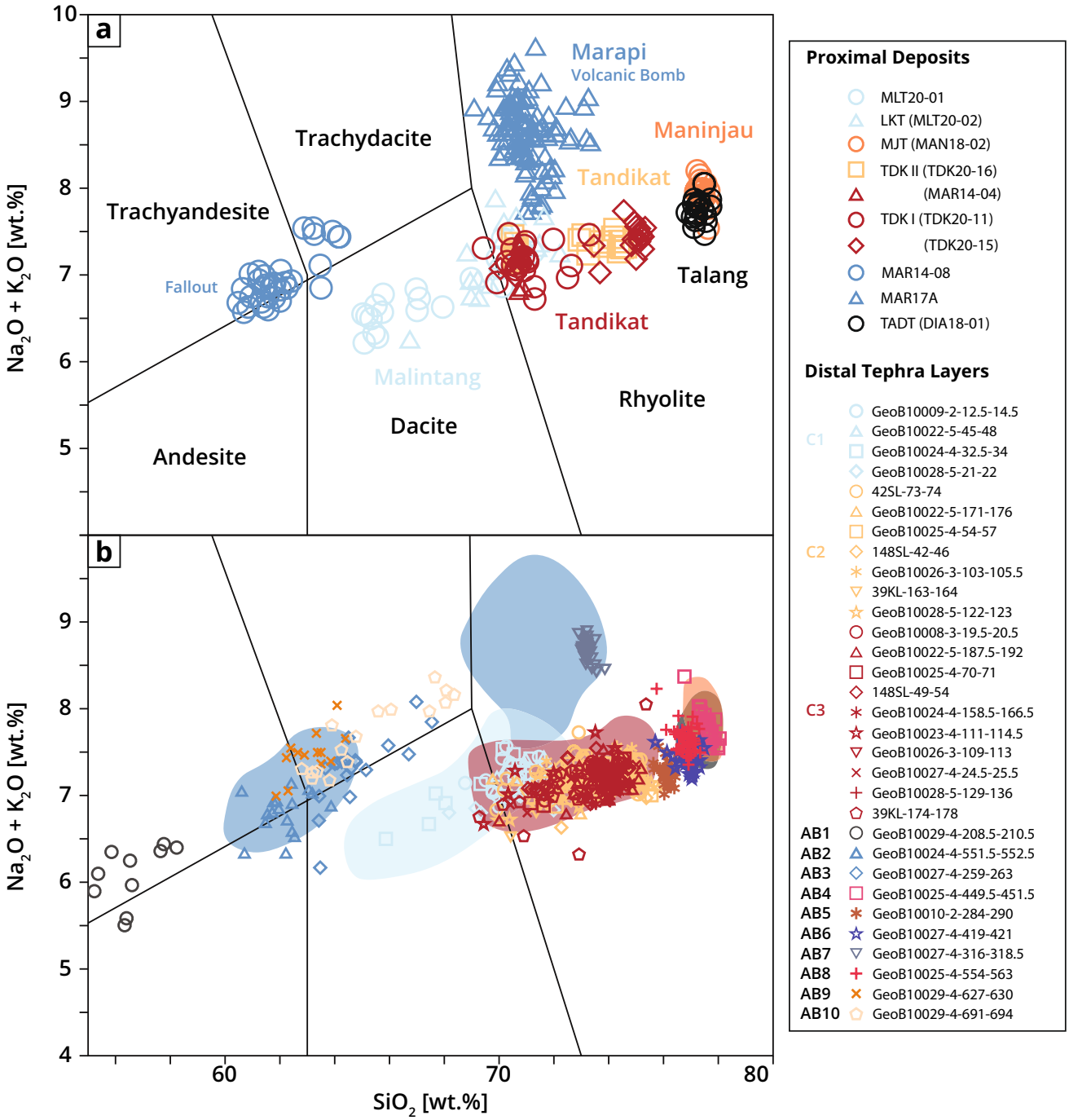

Fig. 2 Total alkali ($Na_2O + K_2O$ wt%) versus silica (SiO_2 wt%) bivariate diagrams showing juvenile glass composition ranges of proximal pyroclastic deposits and distal tephra layers (normalised on a volatile-free basis) with the volcanic rock classification after Le Maitre et al. (2002). **a** Juvenile glass compositions of proximal pyroclastic deposits from West Sumatra. **b** Juvenile glass compositions of correlated distal ash layers (C1–C3) and ash beds (AB1–AB10). The analysed juvenile glass compositions indicated two geochemical trends: (1) a high-alkali trend and (2) a low-alkali trend. Colours and symbols representing each proximal pyroclastic deposit and distal tephra layer are given in the legend

Malintang

MLT20-01 and MLT20-02 were sampled ~ 20 km southwest of the Malintang summit (Fig. 1; Table S1). MLT20-01 was identified in a riverbed on the southwestern flank of Malintang and comprises grey pumices ≤ 30 cm in diameter. MLT20-02 was obtained near the Lubuk King village (Fig. 4a) and consists of a > 70 cm-thick, coarse-grained, well sorted and dark

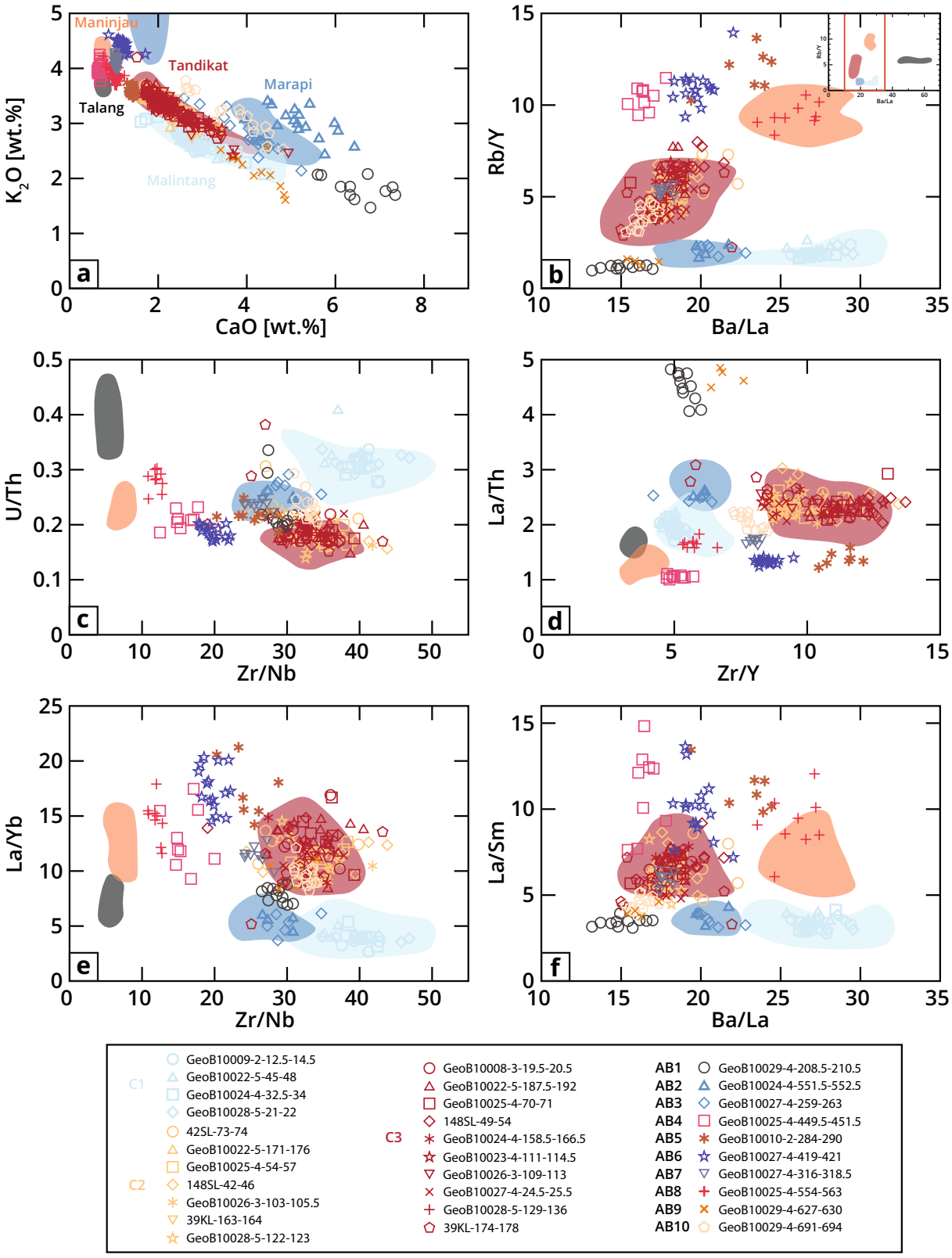

Fig. 3 Bivariate diagrams showing major and trace element juvenile glass compositions of distal ash layers (C1–C3) and ash beds (AB1–AB10), as well as the juvenile glass compositional fields of proximal pyroclastic deposits from West Sumatra. **a** K_2O wt% versus CaO wt% bivariate plot. **b** Rb/Y versus Ba/La bivariate plot. **c** Zr/Nb versus U/Th bivariate plot. **d** La/Th versus Zr/Y. **e** La/Yb versus Zr/Nb bivariate plot. **f** La/Sm versus Ba/La bivariate plot. Colours and symbols representing each ash layer and ash bed are given in the legend

Table 2 Representative juvenile glass compositions for the proximal pyroclastic deposits sampled in the study

Source	Sample	Eruption	Glass type	Representative juvenile glass compositions–major and trace elements content and ratio[#]								
				SiO_2 wt%	K_2O wt%	CaO wt%	Na_2O/K_2O	Ba/La	La/Th	Rb/Y	Zr/Nb	Zr/Y
Malintang	MLT20-01	*Unknown*	Dacite to low-silica rhyolite	65.0–69.2	2.2–2.6	3.3–4.6	1.7–2.0	26.4–29.8	1.8–1.9	1.5–1.7	39.2–44.3	4.1–4.9
	MLT20-02	Lubuk King Tephra (LKT)	Dacite to low-silica rhyolite	69.3–71.3	2.6–2.9	2.5–3.4	1.5–1.7	26.4–29.6	1.8–2.1	1.8–3.0	35.0–40.8	4.9–5.5
Maninjau	MAN18-02	Maninjau Tuff (MJT)	Rhyolite	77.2–77.6	4.4–4.5	0.7–0.8	0.8–0.9	24.1–27.3	1.2–1.4	9.0–10.5	7.1–8.1	3.2–3.8
Tandikat	MAR14-04	Tandikat I Tephra (TDK I)	Low-silica rhyolite	70.9–74.4	2.9–3.5	1.8–3.0	1.1–1.4	15.8–18.7	2.1–2.6	3.6–5.6	30.6–37.2	9.1–11.7
	TDK20-11											
	TDK20-15											
	TDK20-16	Tandikat II Tephra (TDK II)	Low-silica rhyolite	73.8–74.6	3.3–3.6	1.9–2.1	1.1–1.2	17.0–19.3	2.0–2.4	4.8–5.6	31.9–35.7	10.9–11.8
Marapi	MAR14-08	Marapi Fallout (MAR)	Trachyandesite to trachydacite	60.9–62.5	2.4–2.7	4.7–5.4	1.6–1.8	18.9–20.6	2.6–2.9	1.8–2.2	25.1–29.4	5.2–6.0
	MAR17A	2017 Marapi (MAR17)	Rhyolite	70.3–72.0	4.9–6.0	1.4–1.9	0.4–0.7	N/A	N/A	N/A	N/A	N/A
Talang	DIA18-01	Talang Diatas Tuff (TADT)	Rhyolite	77.1–77.5	3.6–4.1	0.7–0.8	0.9–1.1	46.5–60.1	1.6–1.8	5.8–6.2	5.5–6.4	2.9–3.1
Djudjun	KR18-20	Djudjun Tephra (DJT)	Rhyolite	76.0–76.5	3.5–3.6	1.4–1.5	1.0–1.1	19.8–24.6	1.2–1.6	11.1–14.1	17.8–26.4	8.8–13.6
	KR18-41											
	KR18-42											
Ranau	SSU19-08	Ranau Tuff (RAN)	Rhyolite	77.9–78.2	3.1–4.3	0.9–1.6	0.8–1.2	16.1–17.1	0.9–1.0	9.8–12.3	14.4–17.6	5.1–5.9

grey ash fallout deposit overlain by alluvial sediments (hereafter labelled Lubuk King Tephra, LKT). The stratigraphic relationship between the deposits is unclear. Given the location, clast size and thickness of these deposits, as well as the absence of other volcanoes nearby, Malintang is considered the most likely source. Mineral assemblages of these deposits are dominated by plagioclase, orthopyroxene, clinopyroxene, amphibole, Fe-Ti oxide and apatite, whilst juvenile glass compositions range from dacite to low-silica rhyolite (Fig. 2a; Table 2). Compared to other West Sumatra deposits, the Malintang deposits are characterised by the lowest K_2O content, high Zr/Nb and low Rb/Y and La/Yb ratios (Fig. 3; Table 2).

Maninjau

MAN18-02 was collected from a ~ 30-m-thick pyroclastic succession of MJT located ~ 20 km southwest of Maninjau caldera (Fig. 1; Table S1). The massive, poorly sorted, lithic-poor and pumice-rich MJT deposit comprises mainly crystal-poor, frothy and grey pumices ≤ 10 cm in diameter, set within a fine-grained ash matrix (Fig. 4b). The mineral assemblage is dominated by plagioclase, quartz, biotite, Fe-Ti oxide, apatite, zircon and monazite, whilst the juvenile glass composition is rhyolitic with high K_2O and low CaO concentrations, high La/Yb and Rb/Y and low Zr/Nb, La/Th and Zr/Y ratios (Figs. 2a and 3; Table 2).

Marapi

A ~ 60-cm-thick, coarse-grained and poorly sorted lapilli fallout layer (MAR14-08) was sampled ~ 9 km north of the Marapi summit (Figs. 1 and 4c; Table S1). The black scoriaceous lapilli are ≤ 8 cm in diameter and contain plagioclase, orthopyroxene, clinopyroxene and Fe-Ti oxide. The juvenile glass composition ranges from trachyandesitic to trachydacitic with high K_2O content, low La/Yb, La/Sm and Rb/Y and high La/Th ratios (Figs. 2a and 3; Table 2). A comparison between this sample and the summit scoria bombs from the 2017 Marapi eruption (MAR17A; Nurfiani et al. 2021) reveals a notable difference in the major element compositions (Table 2). However, the elevated SiO_2 and K_2O concentrations measured in the residual glasses of the scoria bombs are likely due to syn-eruptive crystallisation as testified by the abundance of groundmass microlites.

Talang

Weathered tuff deposits composed of ~ 10–30-cm-thick, fine-grained and well sorted ash fallout, as well as a ~ 50-cm-thick, coarse-grained, poorly sorted and pumice-rich lapilli tuff, were identified on a road-cut south of Danau (Lake) Diatas (Fig. 1 and 4d; Table S1). Pumice clasts (~ 2–5 cm in

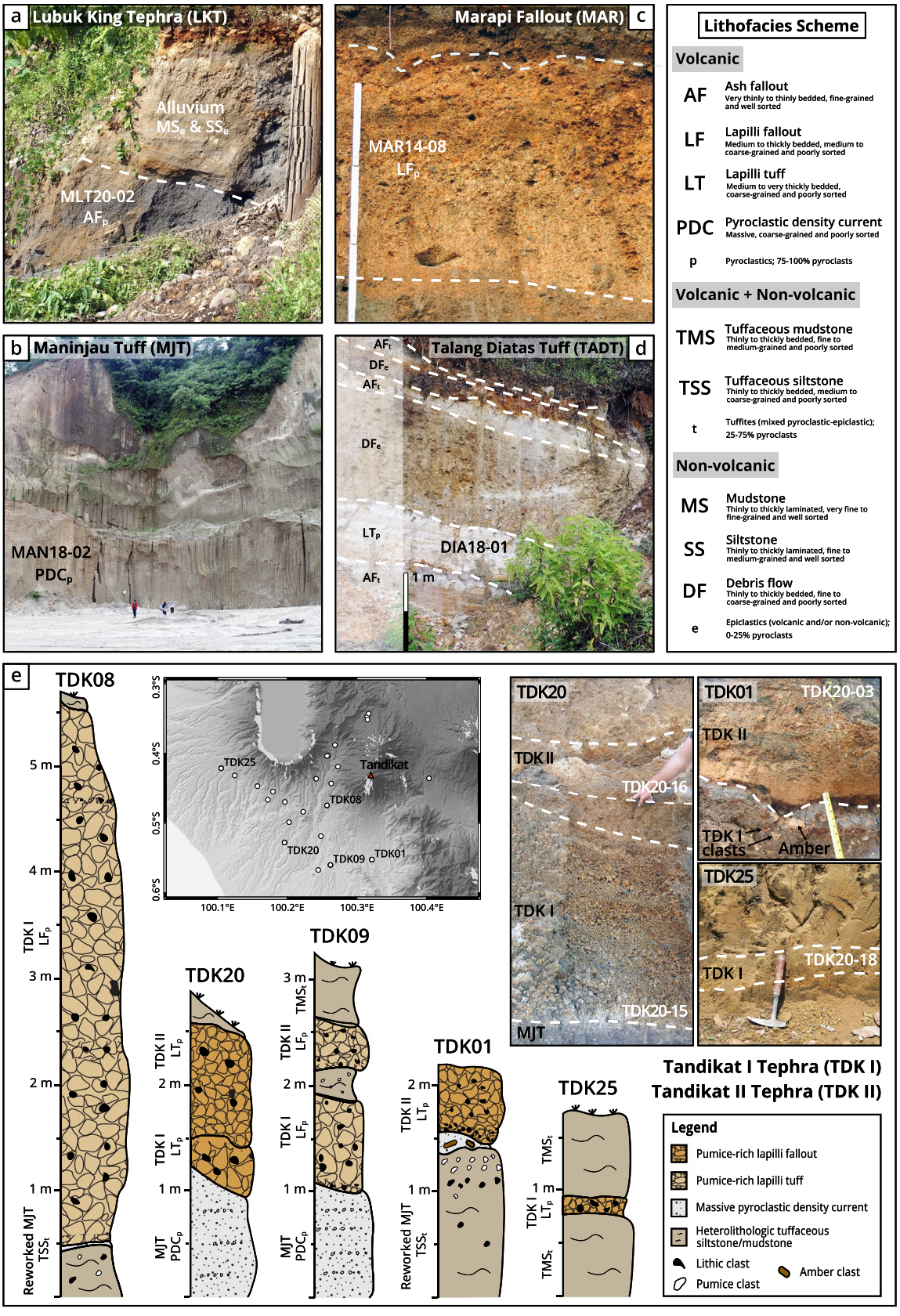
a Lubuk King Tephra (LKT)
Alluvium
MS$_e$ & SS$_e$
MLT20-02
AF$_p$
b Maninjau Tuff (MJT)
MAN18-02
PDC$_p$
c Marapi Fallout (MAR)
MAR14-08
LF$_p$
d Talang Diatas Tuff (TADT)
AF$_t$
DF$_e$
AF$_t$
DF$_e$
LT$_p$
AF$_t$
DIA18-01
1 m
Lithofacies Scheme
Volcanic
AF Ash fallout
Very thinly to thinly bedded, fine-grained and well sorted
LF Lapilli fallout
Medium to thickly bedded, medium to coarse-grained and poorly sorted
LT Lapilli tuff
Medium to very thickly bedded, coarse-grained and poorly sorted
PDC Pyroclastic density current
Massive, coarse-grained and poorly sorted
p Pyroclastics; 75-100% pyroclasts
Volcanic + Non-volcanic
TMS Tuffaceous mudstone
Thinly to thickly bedded, fine to medium-grained and poorly sorted
TSS Tuffaceous siltstone
Thinly to thickly bedded, medium to coarse-grained and poorly sorted
t Tuffites (mixed pyroclastic-epiclastic); 25-75% pyroclasts
Non-volcanic
MS Mudstone
Thinly to thickly laminated, very fine to fine-grained and well sorted
SS Siltstone
Thinly to thickly laminated, fine to medium-grained and well sorted
DF Debris flow
Thinly to thickly bedded, fine to coarse-grained and poorly sorted
e Epiclastics (volcanic and/or non-volcanic); 0-25% pyroclasts
e
TDK08
5 m
4 m
TDK I LF$_p$
3 m
2 m
1 m
Reworked MJT TSS$_t$
0.3°S
0.4°S
0.5°S
0.6°S
100.1°E
100.2°E
100.3°E
100.4°E
TDK25
Tandikat
TDK08
TDK20
TDK09
TDK01
TDK20
TDK II LT$_p$
TDK I LT$_p$
MJT PDC$_p$
TDK09
3 m
TMS$_t$
TDK II LF$_p$
TDK I LF$_p$
MJT PDC$_p$
TDK01
TDK II LT$_p$
Reworked MJT TSS$_t$
TDK25
TMS$_t$
TDK I LT$_p$
TMS$_t$
TDK20
TDK II
TDK20-16
TDK I
TDK20-15
MJT
TDK01
TDK20-03
TDK II
TDK I clasts
Amber
TDK25
TDK20-18
TDK I
Tandikat I Tephra (TDK I)
Tandikat II Tephra (TDK II)
Legend
Pumice-rich lapilli fallout
Pumice-rich lapilli tuff
Massive pyroclastic density current
Heterolithologic tuffaceous siltstone/mudstone
Lithic clast
Pumice clast
Amber clast

◂**Fig. 4** Field photographs of key proximal pyroclastic deposits in West Sumatra. **a** Lubuk King Tuff (LKT) deposit identified in the riverbed of Sungai (River) Batang Bayang southwest of Malintang summit. **b** Maninjau Tuff (MJT) deposit located along the coastline west of the Maninjau caldera. **c** Scoriaceous Marapi Fallout (MAR) deposit sampled north of the Marapi summit. **d** Talang Diatas Tuff (TADT) deposit identified south of Danau (Lake) Diatas. **e** Overview and selected composite stratigraphic sections of TDK01, TDK08, TDK09, TDK20 and TDK25, as well as selected photographs of Tandikat II Tephra (TDK II) and Tandikat I Tephra (TDK I) deposits from stratigraphic sections TDK01, TDK20 and TDK25. Map inset illustrates the locations of TDK II and TDK I outcrops around Tandikat volcano. Nomenclature and classification of the lithofacies scheme established for the key proximal pyroclastic deposits are adopted from Schmid (1981) and Lucchi (2013)

diameter) were sampled from the lapilli tuff layer (DIA18-01; hereafter labelled Talang Diatas Tuff, TADT). The mineral assemblage of the pumices is dominated by plagioclase, quartz, biotite, Fe-Ti oxide, apatite and zircon. Talang is the most likely source for TADT based on its proximity to the outcrop and the absence of other potential sources in the area. The rhyolitic TADT is compositionally like MJT, but with lower K_2O content, higher Ba/La and U/Th and lower Zr/Nb ratios (Figs. 2a and 3; Table 2).

Tandikat

A prominent pyroclastic succession corresponding to the MT previously described by Hosobuchi et al. (2021) and Suhendro (2024) was recognised to the north, east and dominantly to the south and southwest of Tandikat. Twenty-four outcrops were sampled at distances between ~ 6 and 24 km from the volcano (Fig. 1; Table S12) and were either a single coarse-grained, well sorted and pumice-rich lapilli fallout/tuff deposit (22 outcrops) or a succession of two distinct coarse-grained, well-sorted and pumice-rich lapilli/tuff fallout deposits separated by an erosional surface (2 outcrops). For some outcrops, the base of the deposit is marked by a palaeosol. In other cases, the deposit rests unconformably above the MJT (Fig. 4e). Hosobuchi et al. (2021) and Suhendro (2024) described the MT as a single unit with no distinction between the two lapilli fallout/tuff deposits. Consequently, the MT is renamed as newly defined units of Tandikat II Tephra (TDK II) and Tandikat I Tephra (TDK I). Both units are characterised by low-silica rhyolitic juvenile glass that is similar in major and trace element compositions and share the same mineral assemblage of plagioclase, orthopyroxene, clinopyroxene, amphibole, Fe-Ti oxide and apatite (Figs. 2a and 3; Table 2). However, TDK II and I can be clearly distinguished based on the Al_2O_3 content and FeO/MgO ratio of amphibole crystals, which likely reflect different magma storage conditions (Fig. S3 in Online Resource 6; Tables S14-S16 in Online Resource 7). Based on this distinctive feature, most proximal outcrops were assigned as TDK I, whereas TDK II only occurs south of Tandikat (Fig. 4e; Table S1). In comparison to other West Sumatra deposits, TDK II and I display higher Zr/Y and lower U/Th ratios (Fig. 3; Table 2). Several centimetre-size pieces of amber were found at the base of TDK II within a ~ 5–20-cm-thick, poorly sorted and heterolithologic tuffaceous siltstone (reworked MJT; TDK01; Fig. 4e). Radiocarbon dating of the amber produced a median calibrated age of 4303 ± 65 cal a BP (1σ; Fig. 6; Table S10) for TDK II.

Potential sources from neighbouring provinces

A pyroclastic succession was uncovered (hereafter labelled Djudjun Tephra, DJT) south of Danau (Lake) Kerinci and within the Lempur area in Jambi. The DJT identified around Danau Kerinci consists of a ~ 2-m-thick, coarse-grained, well sorted and pumice-rich white lapilli tuff deposit (KR18-20; Table S1), whereas the DJT located within the Lempur area is characterised by a ~ 1.7-m-thick succession of lapilli fallout and PDC deposits composed of white pumices and fine-grained ash (KR18-41 and KR18-42; Table S1). The pumices are crystal-poor and contain plagioclase, amphibole, orthopyroxene, Fe-Ti-oxide, apatite and zircon. The juvenile glass composition is rhyolitic, with very distinct major and trace element compositions (e.g. relatively low K_2O content, as well as high Rb/Y, Zr/Y and La/Yb ratios; Fig. S1; Table 2). The provenance of this deposit is unknown; however, based on its distribution, it is likely sourced from the nearby volcanoes of Raja-Sabanda or Kunyit (Fig. S4 in Online Resource 6).

The Ranau Tuff (RAN) is a product of the caldera-forming eruption at Ranau caldera located on the southernmost sector of the Sumatran Fault. The associated pyroclastic succession was recognised ≤ 70 km from the source with a thickness of several metres in South Sumatra (Natawidjaja et al. 2017). Deposits of the RAN were sampled ~ 17 km southeast of the caldera (SSU19-08; Table S1). In this outcrop, the RAN consists of ~ 15-m-thick, poorly sorted, pumice-rich PDC deposits with crystal-rich white pumices ≤ 50 cm in diameter, set within a coarse-grained ash matrix. The mineral assemblage is composed of plagioclase, quartz, biotite, Fe-Ti-oxide, apatite and zircon, whereas the juvenile glass composition is rhyolitic—similar in major element composition to the MJT and TADT, but with different trace element signatures (i.e. lower Rb/Y, as well as higher La/Sm and Zr/Nb ratios; Fig. S1; Table 2). A proposed eruption age of 34,011 ± 177 cal a BP (1σ; recalibrated median age using SHCal20 curve; Table S9) was determined for RAN via radiocarbon dating of organic material sampled at the base of the proximal deposit (Natawidjaia et al. 2017).

Distal tephra record

Forty-six ash beds were sampled from 14 deep-sea cores. Out of these, 31 primary ash beds characterised by homogeneous

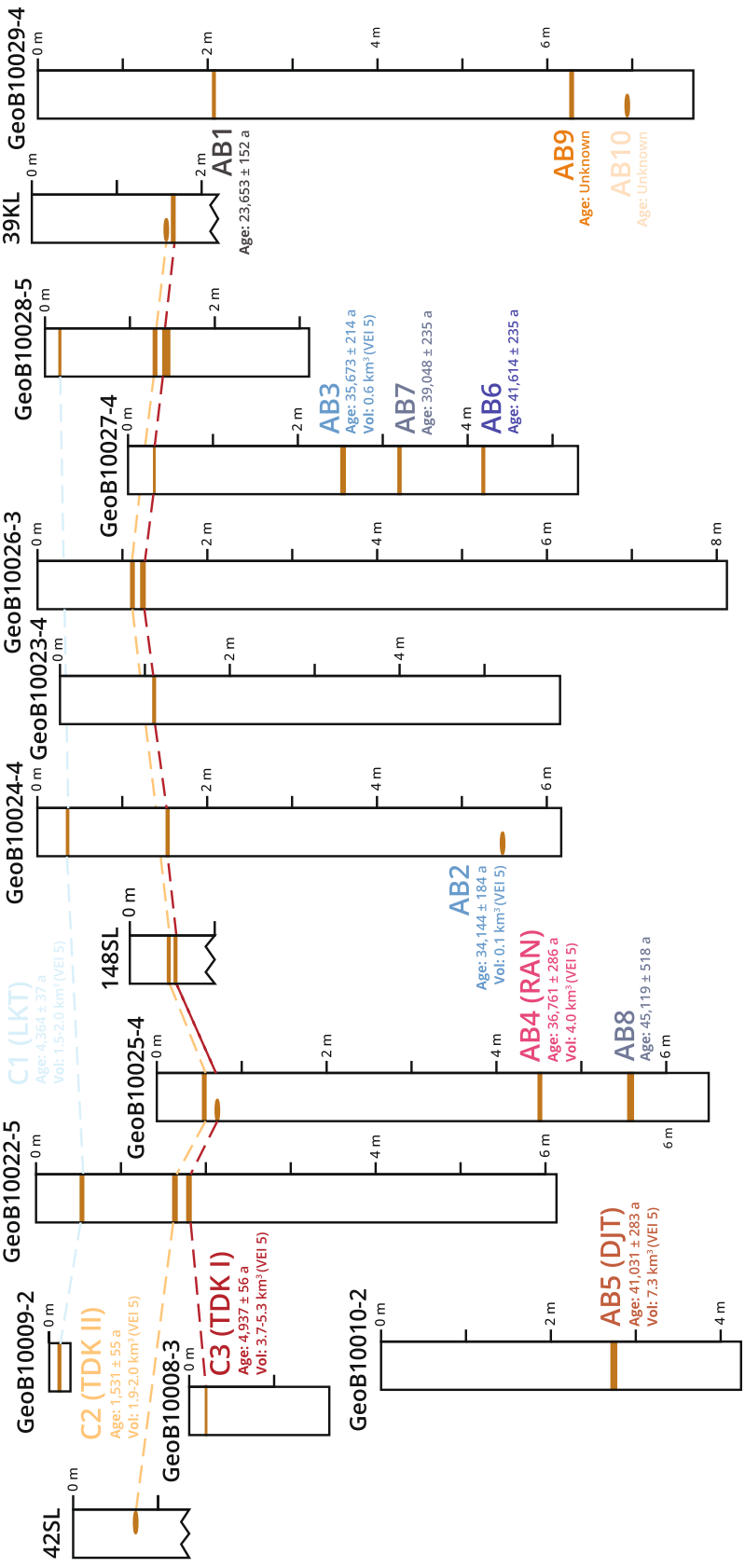

Fig. 5 Schematic stratigraphy of 31 primary distal tephra layers, i.e. ash layers (C1–C3) and ash beds (AB1–AB10) within 14 deep-sea cores utilised in the study. Ash layers C1–C3 provide chronostratigraphic links between the core sites offshore of West Sumatra. Core sites are arranged from North (left) to South (right). Ash layers C1–C3 and ash beds AB4–AB5 correlate to specific proximal deposits. Ash beds AB2–AB3 are correlated to a specific source volcano. The remaining ash beds are uncorrelated with unknown source provenances. Coloured dash lines represent ash layers that are correlated across the suite of deep-sea cores

or zoned glass compositions were identified. The primary ash beds are generally white, light to dark grey, black or "salt-and-pepper" in colour. Textural characteristics of these ash beds (i.e. well-sorted nature, sharp basal boundaries and diffusive upper contacts) are typical of fallout deposits from subaerial eruptions that settled rapidly within a water column, whilst their grain sizes vary widely from fine to coarse-grained ash. Volcanic glass shards associated with the white to light grey ash beds are often clear and colourless and mainly intermediate to felsic in composition, whereas glass shards occurring within the dark grey to black ash beds are generally light brown to brown in colour and mostly intermediate to mafic in composition. Glass shard morphologies span a wide range including flat, blocky, curviplanar, fibrous and cuspate shapes, with rounded to elongated vesicles. The remaining 15 secondary (or reworked) ash beds were characterised by heterogenous glass compositions and exhibited clear signs of physical disturbances (i.e. presence of burrow structures, as well as chaotic and mixed layers) that are attributable to re-sedimentation processes such as bioturbation and turbidity currents.

Tephra correlations, provenances, volumes and eruption ages

Thirty-one primary ash beds underwent tephra correlation procedures that revealed three widespread ash layers (C1–3) correlated across multiple coring locations and ten ash beds (AB1–10) that were only present in singular cores. Correlations established across the various core sites, as well as their preferred eruption ages, volumes and sizes (VEI), are summarised in Fig. 5. Glass chemistry of the correlated ash beds/layers spans a wide range from andesitic to rhyolitic, with most glass shards predominantly low-silica rhyolitic in nature (Fig. 2b). The representative juvenile glass compositions for each ash bed/layer are presented in Table 3.

C1

C1 was identified in three cores (GeoB10022-5, GeoB10024-4 and GeoB-10028–5) located in the northern Mentawai basin and within one core (GeoB10009-2) situated on the accretionary prism southwest of Pulau Tanahbala (Fig. 1 and 5; Table S2). C1 is a vitric, fine-grained and reddish-brown ash horizon characterised by dacitic to low-silica rhyolitic juvenile glass that ranges in thickness between 1 and 3 cm (Fig. 2b; Table 3). The stratigraphic depth of C1, as well as the similarity in juvenile glass chemistry with V-4 (Salisbury et al. 2012; Fig. S2) and the proximal ash fallout deposit (MLT20-02), reveals a correlation with the LKT (Fig. 3). These stratigraphic and geochemical correlations are validated by the PCA and MEHCA analyses as observed in Figs. 7 and 8. Radiocarbon median calibrated ages of 1581 ± 110, 1569 ± 110 and 1438 ± 101 cal a BP (1σ) were obtained for C1 from cores GeoB10022-5, GeoB10024-4 and GeoB10028-5 respectively (Fig. 6; Tables S9 and S10). These radiocarbon ages, along with the recalibrated interpolated age of 1539 ± 117 cal a BP (1σ) from core RR0705-79PC (Salisbury et al. 2012), overlap well within 2 sigma uncertainties (Fig. 6; Tables S9 and S10). Correspondingly, a weighted mean age (and preferred eruption age) of 1531 ± 55 a (1σ; $n = 4$) was obtained for C1 (LKT) (Figs. 5 and 6). Distal isopachs of 3 and 1 cm were constructed using five thickness data points, with resulting areas of $\sim 1.7 \times 10^4$ and $\sim 5.5 \times 10^4$ km^2, respectively (Fig. 9a; Table S11). A minimum volume range of ~ 1.9–2.0 km^3, corresponding to a VEI 5 eruption, was calculated for C1 (LKT) using the method of Legros (2000) (Fig. 5 and Table S11).

C2 and C3

C2 and C3 were identified in tandem within six cores (GeoB10022-5, GeoB10025-4, GeoB10026-3, GeoB10028-5, 148SL and 39KL) from the northern Mentawai basin, whereas either ash layer C2 or C3 were identified as a singular ash horizon within five other cores in the region (Figs. 1 and 5; Table S2). Specifically, only C2 was recognised in core 42SL from the Nias basin, whilst only C3 was identified within cores GeoB-10008–3, GeoB10023-4, GeoB10024-4 and GeoB10027-4 from the Mentawai basin (Figs. 1 and 5; Table S2). C2 is a vitric, fine-grained and grey ash ranging in thickness between 1 and 5 cm, whereas C3 is a vitric-crystalline, coarse-grained and "salt-and-pepper" ash with a thickness ranging from 1 to 8 cm (Table 3). Juvenile glasses in C2 and C3 are low-silica rhyolites and significantly, their major and trace element compositions are indistinguishable from each other (Figs. 2b and 3; Table 3). These geochemical signatures overlap with the proximal TDK II and I deposits (supported by PCA and MEHCA analyses; Figs. 7, 8 and S2), as well as V-5 (Salisbury et al. 2012), for which a median calibrated age range between 4215 ± 109 and 4823 ± 123 cal a BP (1σ; recalibrated median ages using Marine20 curve; Fig. 6; Table S10) was proposed.

Within cores where both ash layers are present, a median calibrated age range between 4276 ± 127 and 4570 ± 125 cal a BP (1σ) was obtained for C2 and a median calibrated age range from 4665 ± 120 to 5177 ± 126 cal a BP (1σ) was attained for C3 (Fig. 6; Table S10). In the cores where only singular ash layers occur, derived median calibrated ages mostly overlap with C3 (between 4858 ± 131 and 5153 ± 126 cal a BP (1σ); cores GeoB10008-3, GeoB10023-4 and GeoB10024-4), except for the median calibrated age of 4451 ± 131 cal a BP (1σ) from core 42SL that overlaps well with C2 (Fig. 6; Table S10). A re-examination of the radiocarbon ages provided by Salisbury et al. (2012) indicates that C2 and C3 were likely misrepresented as a singular V-5 layer. It is likely that the recalibrated interpolated

Table 3 Representative juvenile glass compositions for the distal tephra layers sampled in the study

Tephra	Eruption	Core	Sample interval*	Glass type	Representative juvenile glass compositions–major and trace elements content and ratio#								
					SiO_2 wt%	K_2O wt%	CaO wt%	Na_2O/K_2O	Ba/La	La/Th	Rb/Y	Zr/Nb	Zr/Y
C1	LKT	GeoB10009-2	12.5–14.5	Dacite to low-silica rhyolite	69.2–71.5	2.5–2.8	2.5–3.3	1.6–1.8	26.2–28.4	1.8–2.1	1.7–2.2	37.1–42.8	4.7–5.3
		GeoB10022-5	45–48										
		GeoB10024-4	32.5–34										
		GeoB10028-5	21–22										
C2	TDK II	42SL	73–74	Low-silica rhyolite	72.3–74.9	3.2–3.6	1.8–2.5	1.0–1.3	16.4–20.8	2.1–2.7	3.7–6.7	28.0–37.2	8.0–11.1
		GeoB10022-5	171–175.5										
		GeoB10025-4	54–57										
		148SL	42–46										
		GeoB10026-3	103–105.5										
		39KL	163–164										
		GeoB10028-5	122–123										
C3	TDK I	GeoB10008-3	19.5–20.5	Low-silica rhyolite	72.1–75.1	3.1–3.6	1.7–2.6	1.0–1.3	16.3–20.9	2.1–2.5	4.4–6.9	27.9–36.6	9.1–12.6
		GeoB10022-5	187.5–192										
		GeoB10025-4	70–71										
		148SL	49–54										
		GeoB10024-4	158.5–166.5										
		GeoB10023-4	111–114.5										
		GeoB10026-3	109–113										
		GeoB10027-4	24.5–25.5										
		GeoB10028-5	129–136										
		39KL	174–178										
AB1	*Unknown*	GeoB10029-4	208.5–210.5	Trachyandesite	55.8–59.7	1.7–2.8	4.9–6.9	1.5–2.4	13.7–17.1	4.3–4.9	1.1–1.5	25.6–29.2	5.1–5.7
AB2	*Marapi*	GeoB10024-4	551.5–552.5		61.3–63.0	2.6–3.2	4.4–6.1	1.1–1.5	19.5–21.2	2.5–2.6	1.8–2.4	27.0–30.8	5.7–6.2
AB3	*Marapi*	GeoB10027-4	259–263		63.7–65.4	2.6–3.0	3.7–4.4	1.5–1.8	20.4–22.5	2.5–2.7	2.1–2.8	25.5–30.4	5.7–6.6
AB4	RAN	GeoB10025-4	449.5–451.5	Rhyolite	77.5–78.0	3.9–4.1	0.6–0.7	0.9–1.0	15.8–17.2	1.0–1.1	9.8–11.1	13.8–18.2	4.8–5.4
AB5	DJT	GeoB10010-2	284–290		76.1–76.4	3.5–3.7	1.4–1.5	1.0–1.1	21.3–24.0	1.3–1.5	11.3–13.6	21.3–25.5	10.9–12
AB6	*Unknown*	GeoB10027-4	419–421		76.7–77.3	4.3–4.5	1.2–1.3	0.6–0.7	19.0–21.1	1.3–1.5	9.8–16.5	17.0–20.5	8.2–9.9
AB7	*Unknown*	GeoB10027-4	316–318.5		73.1–73.5	4.1–4.2	1.0–1.1	1.0–1.1	17.3–18.1	1.7–1.8	5.1–5.6	24.4–27.3	7.8–8.2
AB8	*Unknown*	GeoB10025-4	554–563		76.6–77.3	3.8–4.0	0.9–1.1	0.9–1.0	24.5–27.2	1.6–1.7	8.8–10.1	11.2–12.7	5.4–6.1
AB9	*Unknown*	GeoB10029-4	627–630	Trachydacite	62.4–63.9	1.9–2.5	3.7–4.7	2.0–3.0	15.4–17.1	4.5–4.8	1.3–1.6	27.6–33.2	6.4–7.4
AB10	*Unknown*	GeoB10029-4	691–694		63.6–68.2	2.8–3.7	2.7–4.3	1.2–1.7	15.8–16.8	2.0–2.3	3.3–4.2	29.7–33.5	7.4–8.3

*Sample interval measured in centimetres (cm); #average value ± 2 standard deviation

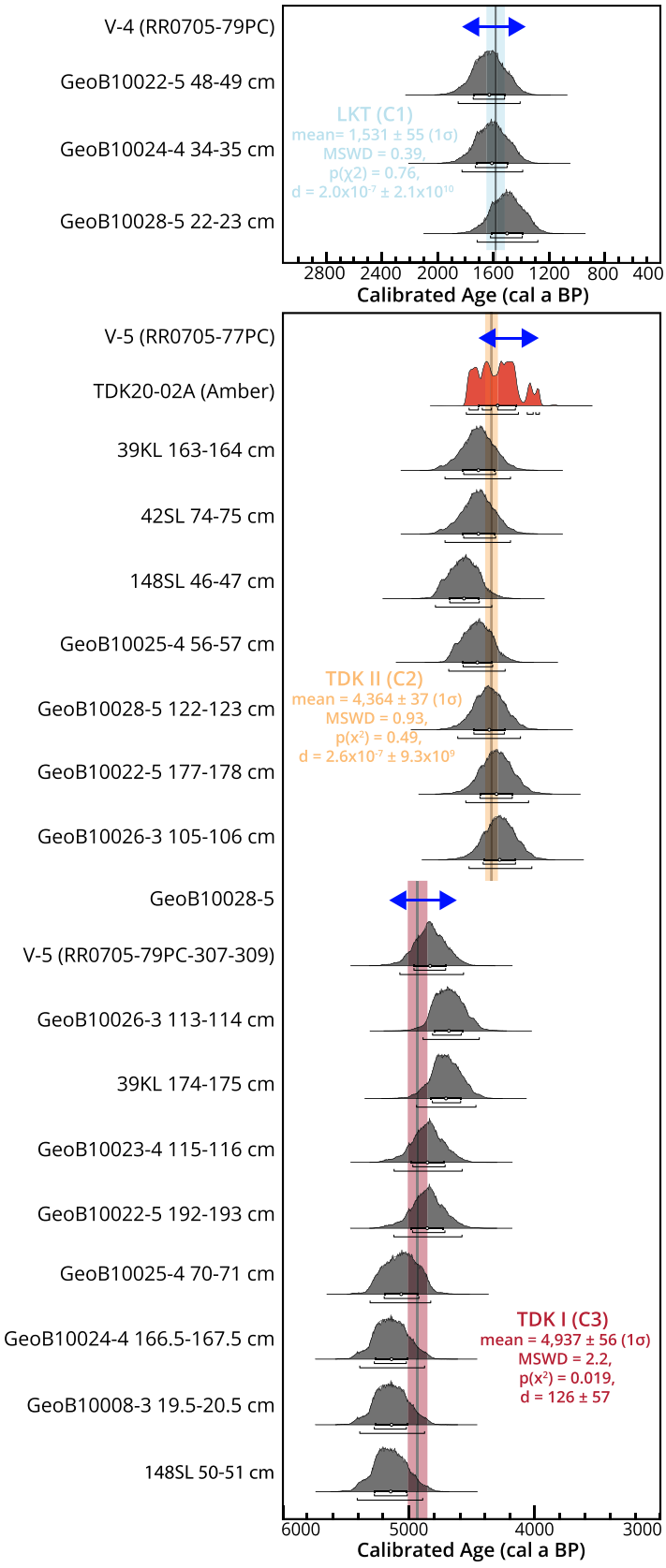

Fig. 6 Calibrated radiocarbon (^{14}C) ages of sediment intervals below and/or within distal ash layers C1 to C3 as ranked order plots. Deep-sea ^{14}C ages were calibrated using OxCal 4.4 (Bronk Ramsey 2009) with the Marine20 calibration curve (Heaton et al, 2020), along with a ΔR correction of −117 ± 70 years (Southon et al. 2002) to account for the marine radiocarbon reservoir effect. The preferred eruption ages for C1 to C3 were determined based on the weighted mean ages of the calibrated ^{14}C ages using IsoplotR (Vermeesch 2018). Weighted mean ages (grey lines) and error ranges (1 sigma) are indicated in light blue for LKT (C1), light orange for TDK II (C2), and red for TDK I (C3). The calibrated 14C age (using the SHCal20 calibration curve; Hogg et al. 2020) for the amber (dark red) sampled below proximal TDK II overlaps well with the weighted mean age of C2. The age ranges for V-4 and V-5 (Salisbury et al. 2012) were recalibrated in the study. The dark blue arrows are estimated ages based on sediment accumulation rates (SAR)

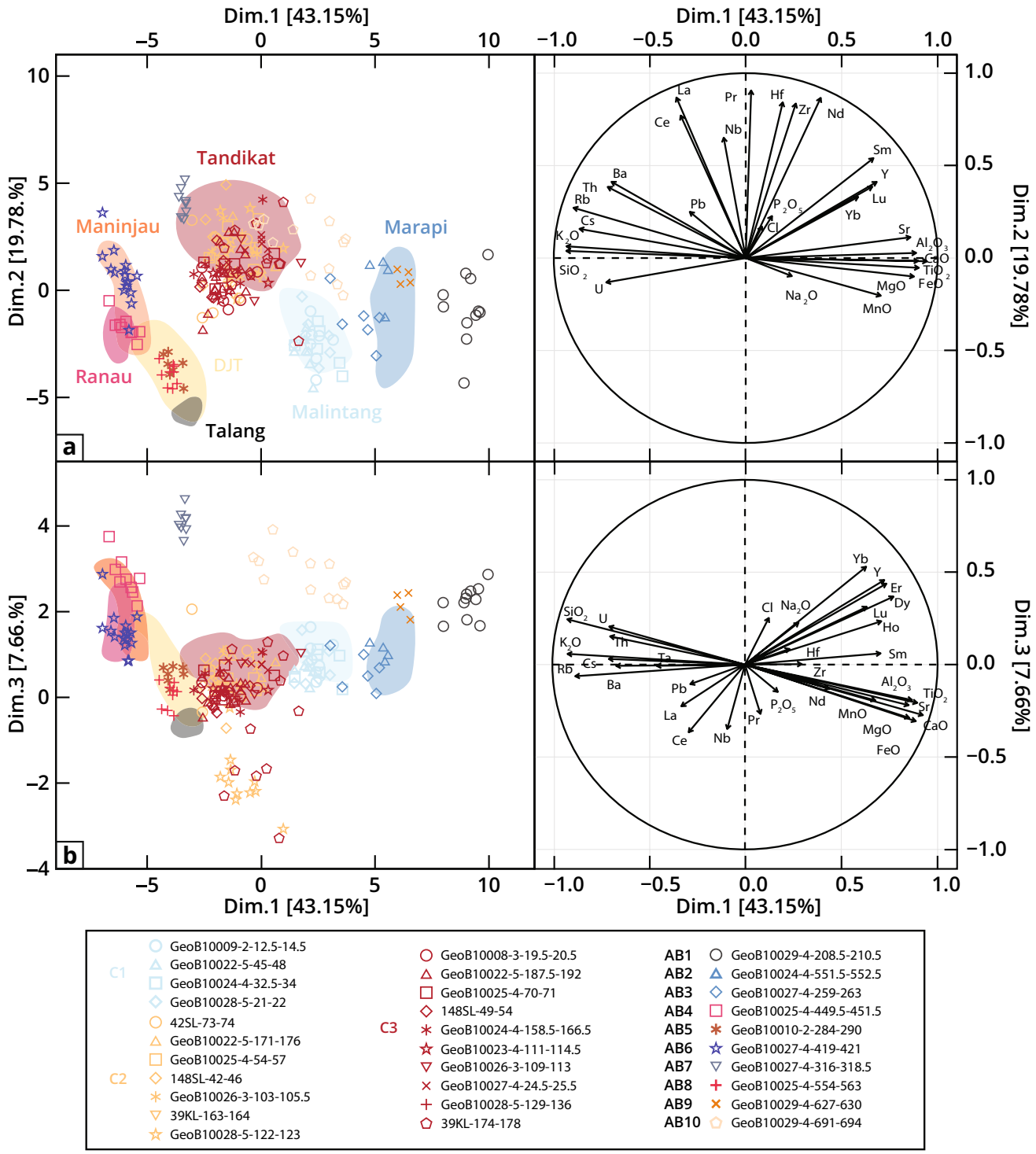

Fig. 7 PCA and loading plots of the three main principal components (DIM.1, DIM.2 and DIM.3) based on the analysis of 37 major and trace elements, which accounts for 70.6% of the total variation in the dataset. a) DIM.2% versus DIM.1% PCA and loading plots. b) DIM.3% versus DIM.1% PCA and loading plots. PCA fields for proximal deposits from West Sumatra, Jambi and South Sumatra are shown for reference. The PCA successfully validates stratigraphic and geochemical correlations between the proximal deposits and distal tephra layers. Colours and symbols representing each ash layer and ash bed are given in the legend

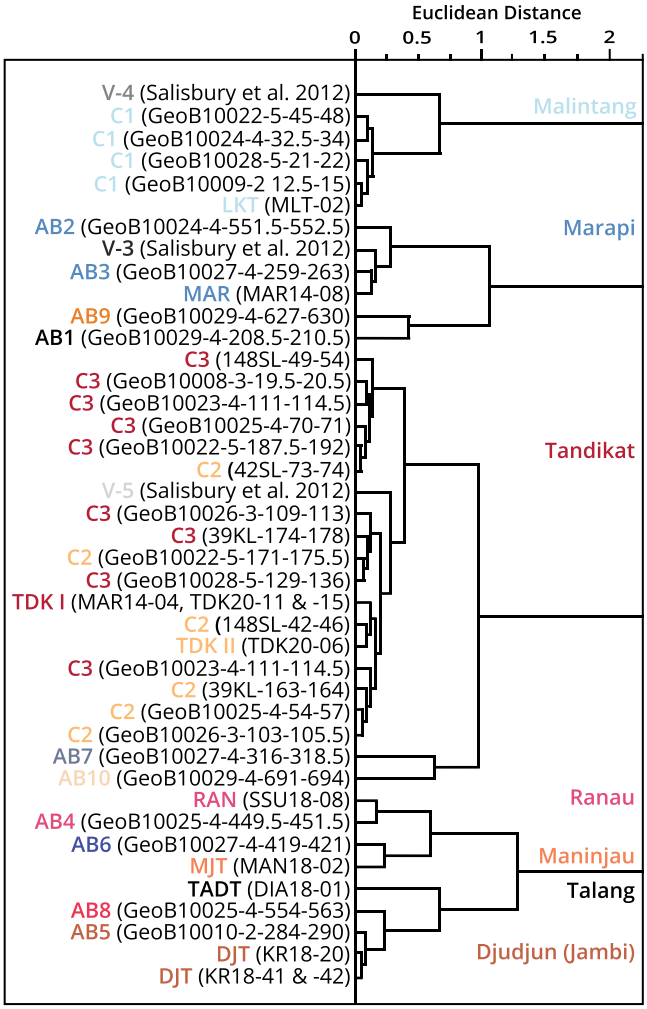

Fig. 8 Dendrogram of multi-element hierarchical cluster analysis (MEHCA; distance metric: squared Euclidean distance; linkage method: Ward). The 41 samples included in the MEHCA are average glass compositions of 9 proximal deposits and 32 distal tephra layers. The MEHCA successfully verifies most stratigraphic relationships except for samples from Tandikat (proximal deposits: TDK II and TDK I; distal ash layers: C2 and C3) that are too similar compositionally to be discriminated clearly. Colours representing each proximal deposit and distal tephra layer are given in the legend of Figure 7

age of 4215 ± 109 cal a BP (1σ) for V-5 obtained from core RR0705-77PC corresponds to C2, whilst the recalibrated median age of 4823 ± 123 cal a BP (1σ) for V-5 determined in core RR0705-79PC corresponds to C3 (Fig. 6; Tables S9 and S10). Textural characteristics of C2 and C3 are analogous to those described for the proximal TDK II and I. Specifically, TDK II deposits are generally finer-grained compared to TDK I, and both deposits are often separated by either heterolithologic tuffaceous siltstones/mudstones (reworked deposits; TDK09; Fig. 4e) or erosional unconformities (TDK20; Fig. 4e). The radiocarbon median calibrated age of 4303 ± 65 cal a BP (1σ) for the amber preserved in the sediments directly below TDK II coincides with the median calibrated age range for C2 (Fig. 6; Tables S9 and S10), thus supporting the observed field stratigraphic relationships (Fig. 4e). Weighted mean ages (and preferred eruption ages) for C2 (TDK II) and C3 (TDK I) are 4364 ± 37 cal a BP (1σ; $n = 9$) and 4937 ± 56 cal a BP (1σ; $n = 10$), respectively (Figs. 5 and 6).

Seventeen thickness data points including six obtained from Salisbury et al. (2012) were utilised to produce the isopachs for C2 (TDK II) and C3 (TDK I) (Fig. 9a). Isopachs of 3, 2 and 1 cm were constructed with areas of ~ 8.5×10^3, ~ 2.4×10^4 and ~ 5.1×10^4 km^2 for TDK II, as well as ~ 1.7×10^4, ~ 3.8×10^4 and ~ 6.2×10^4 km^2 for TDK I (Table S11). Minimum volume ranges obtained for TDK II and I with the method of Legros (2000) were ~ 0.9–1.9 and ~ 1.9–2.6 km^3, respectively, whereas volume ranges derived using the exponential and Weibull methods were ~ 1.5–2.0 and ~ 1.9–2.5 km^3, respectively. The range of volumes estimated for TDK II and I based on the distal dataset with the three methods is in good agreement, corresponding to VEI 5 eruptions (Fig. 5 and Table S11).

TDK I is the only eruption with sufficient proximal data that allows for the estimation of ESP using TError (Table S13). Twenty-two proximal stratigraphic sections (Fig. 4e; Table S12) were investigated to reconstruct the isopach and isopleth maps (Figs. 9b, c) required to characterise the eruptive conditions. Table 4 summarises the ESP for TDK I as determined with the 0.5, 1.5 and 2.0 cm isopleth datasets by using the median, 2nd and 98th percentile as the central value,

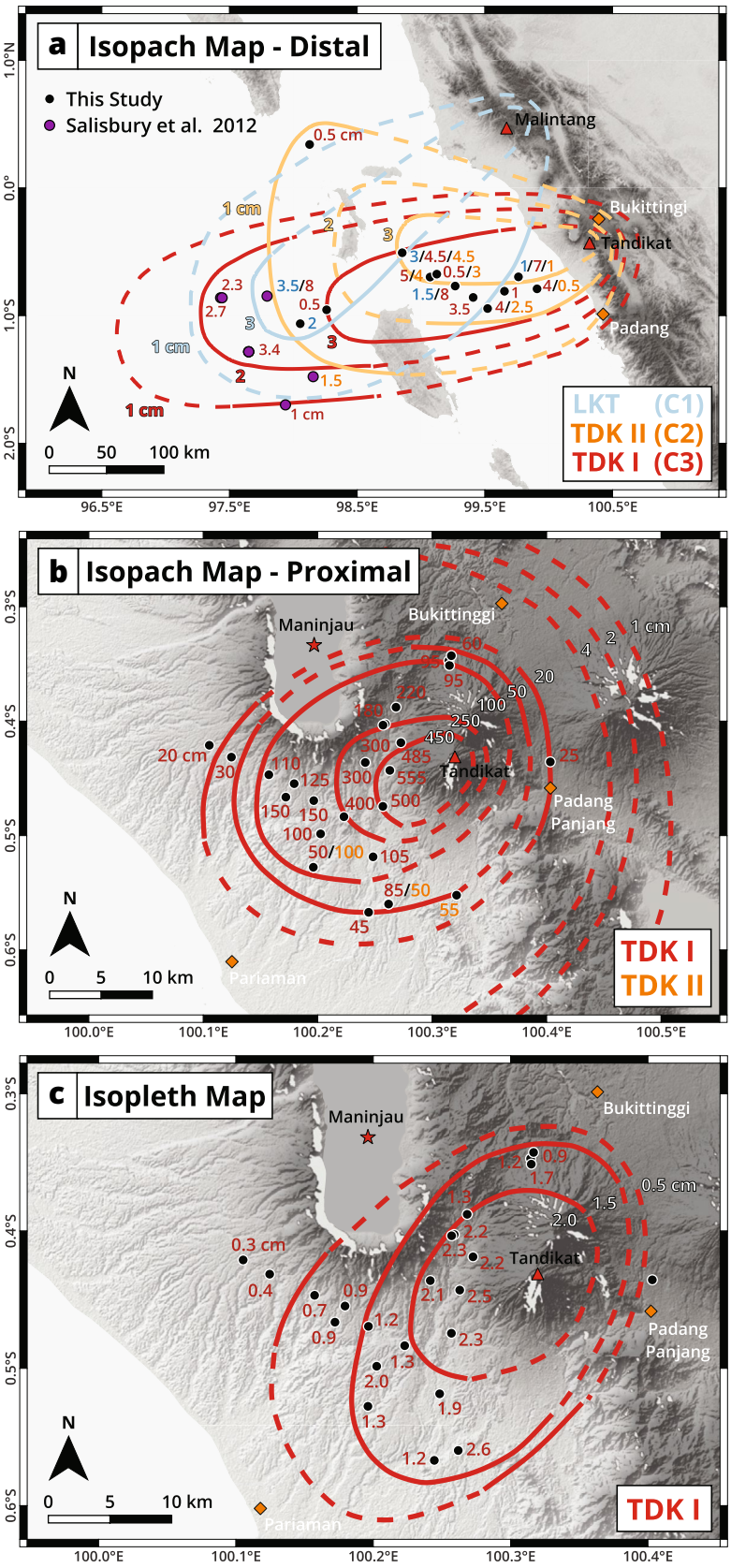

Fig. 9 Isopach and isopleth maps illustrated for the deposits of LKT (C1), TDK II (C2) and TDK I (C3). **a** Isopach maps for the distal ash layer C1 from Malintang volcano, as well as the distal ash layers C2 and C3 from Tandikat volcano (thickness measurements in centimetres). **b** Isopach map for the proximal deposits of TDK II and TDK I from Tandikat volcano (thickness measurements in centimetres). **c** Isopleth map for the proximal deposit of TDK I from Tandikat volcano (average lithic clast diameter in centimetres)

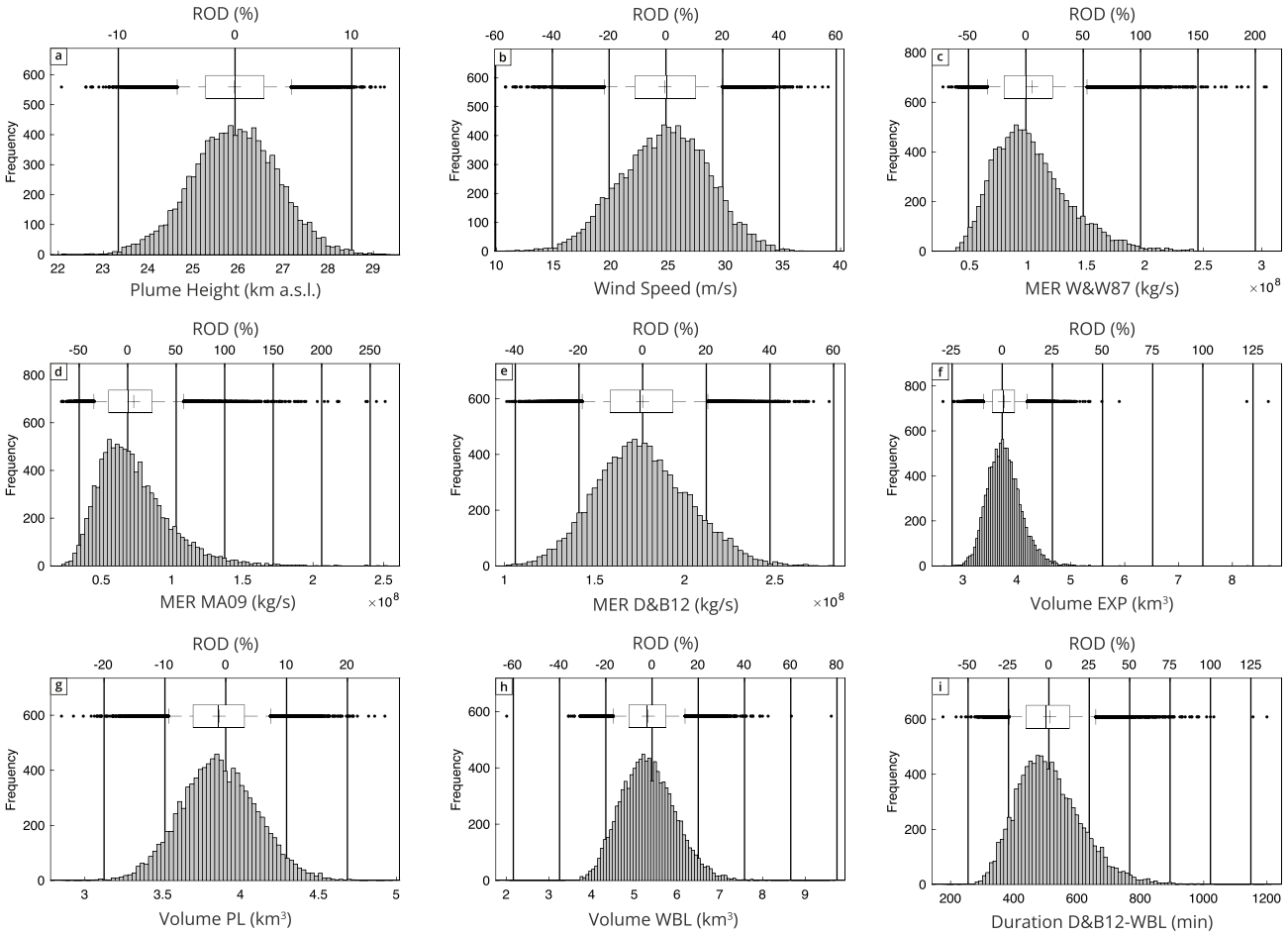

Fig. 10 Distribution of selected eruption source parameters (ESP) resulting from the TError analysis using the 1.5 cm isopleth dataset. **a, b** Plume height and wind speed calculated with the method of Carey and Sparks (1986). **c – e** Mass eruption rates (MER) calculated with the methods of W&W87, Wilson and Walker (1987); MA09, Mastin et al. (2009); and D&B12, Degruyter and Bonadonna (2012), respectively. **f – h** Volumes calculated with the exponential (EXP) method of Fierstein and Nathenson (1992), power law (PL) method of Bonadonna and Houghton (2005) and Weibull (WBL) method of Bonadonna and Costa (2012), respectively. **i** Duration is calculated as the ratio between the mass (converted from the volume obtained with the WBL method) (Bonadonna and Costa 2012) and MER (Degruyter and Bonadonna 2012). ROD (%) refers to the relative output deviations. Central value denotes the median and the lower and upper boundaries represent the 2nd and 98th percentiles that describe 96% of the population

lower and upper bound, respectively, to account for 96% of the population. Given the larger quantity of proximal data associated with the 1.5 cm isopleth (i.e. greater confidence), the corresponding ESP obtained for TDK I were preferred (see distributions of selected ESP for TDK I in Fig. 10). TError results indicated eruptive conditions for TDK I characterised by a plume height of $25.9^{+1.9}_{-2.0}$ km above sea level (a.s.l.); a maximum wind speed of $21.3^{+6.5}_{-6.1}$ m/s at the tropopause; a maximum *MER* of $1.8^{+0.5}_{-0.5} \times 10^8$ kg/s; a volume between $3.7^{+0.8}_{-0.5}$ and $5.3^{+1.4}_{-1.1}$ km^3, depending on the adopted method; and a duration between 6^{+3}_{-2} and 9^{+3}_{-6} hours (Degruyter and Bonadonna 2012). TError-derived volume ranges for TDK I using the proximal and distal datasets are comparatively larger than those obtained with only the distal data, but the eruption remains classified as VEI 5 (Fig. 5 and Table S11).

AB1–AB10

AB1 is a 2-cm-thick, vitric, fine-grained and black ash horizon sampled in core GeoB10029-4 from the central Mentawai basin (Figs. 1 and 5; Table S2). Juvenile glass in AB1 exhibits a trachyandesitic composition with low Ba/La and high La/Th ratios that do not correlate to any known proximal sources (Figs. 2b and 3; Table 3). The radiocarbon median calibrated age obtained for AB1 is 23,653 ± 152 cal a BP (1σ; Table S10).

AB2 is a vitric, fine-grained and black ash pod, whilst AB3 is a 4-cm-thick, vitric, medium-grained and light grey to black ash horizon; these medium-grained ash beds were identified in cores from the northern Mentawai basin (GeoB10024-4 and GeoB10027-4, respectively; Figs. 1 and 5; Table S2). Juvenile glass compositions of AB2 and AB3 range from

Table 4 TDK I, Tandikat volcano: Characterisation of eruption source parameters (ESP) describing 96% of the population, i.e. the 2nd −98th percentile range for the 0.5 cm, 1.5 cm and 2.0 cm isopleth dataset

ESP	Unit	Interpercentile error ranges		
		0.5 cm	1.5 cm	2.0 cm
Plume height (C&S86)	km	$26.2^{+1.9}_{-2.1}$	$25.9^{+1.9}_{-2.0}$	$22.0^{+1.5}_{-1.7}$
Wind speed (C&S86)	m/s	$24.8^{+7.4}_{-8.0}$	$21.3^{+6.5}_{-6.1}$	$18.0^{+6.2}_{-6.2}$
MER (W&W87)	$\times 10^8$ kg/s	$1.00^{+1.00}_{-0.50}$	$0.98^{+0.90}_{-0.50}$	$0.47^{+0.40}_{-0.20}$
MER (MA09)	$\times 10^8$ kg/s	$0.71^{+0.70}_{-0.30}$	$0.69^{+0.70}_{-0.30}$	$0.30^{+0.30}_{-0.20}$
MER (D&B12)	$\times 10^8$ kg/s	$1.70^{+0.50}_{-0.50}$	$1.80^{+0.50}_{-0.50}$	$0.66^{+0.20}_{-0.20}$
Volume (EXP)	km^3	$3.7^{+0.8}_{-0.5}$	$3.7^{+0.8}_{-0.5}$	$3.7^{+0.8}_{-0.5}$
Volume (PL)	km^3	$3.9^{+0.5}_{-0.5}$	$3.9^{+0.5}_{-0.5}$	$3.9^{+0.5}_{-0.5}$
Volume (WBL)	km^3	$4.0^{+1.6}_{-1.1}$	$5.3^{+1.4}_{-1.1}$	$5.3^{+1.4}_{-1.2}$
Mass (EXP)	$\times 10^{12}$ kg	$3.70^{+1.00}_{-0.70}$	$3.70^{+1.00}_{-0.70}$	$3.70^{+1.00}_{-0.70}$
Mass (PL)	$\times 10^{12}$ kg	$3.80^{+0.80}_{-0.60}$	$3.90^{+0.70}_{-0.70}$	$3.80^{+0.80}_{-0.60}$
Mass (WBL)	$\times 10^{12}$ kg	$4.00^{+1.70}_{-1.20}$	$5.30^{+1.60}_{-1.30}$	$5.30^{+1.60}_{-1.30}$
Duration (W&W87-EXP)	h	10^{+10}_{-5}	11^{+10}_{-5}	22^{+21}_{-11}
Duration (W&W87-PL)	h	10^{+10}_{-5}	11^{+10}_{-5}	23^{+21}_{-11}
Duration (W&W87-WBL)	h	11^{+11}_{-6}	15^{+15}_{-8}	31^{+31}_{-16}
Duration (MA09-EXP)	h	15^{+14}_{-8}	15^{+15}_{-8}	33^{+32}_{-17}
Duration (MA09-PL)	h	15^{+15}_{-8}	16^{+15}_{-8}	33^{+31}_{-17}
Duration (MA09-WBL)	h	16^{+18}_{-8}	21^{+23}_{-11}	46^{+46}_{-24}
Duration (D&B12-EXP)	h	6^{+3}_{-2}	6^{+3}_{-2}	16^{+8}_{-5}
Duration (D&B12-PL)	h	6^{+3}_{-2}	6^{+3}_{-2}	16^{+7}_{-5}
Duration (D&B12-WBL)	h	7^{+4}_{-2}	9^{+3}_{-6}	22^{+12}_{-7}

C&S86: Carey and Sparks (1986); W&W87: Wilson and Walker (1987); MA09: Mastin et al. (2009); D&B12: Degruyter and Bonadonna (2012); *EXP*, Fierstein and Nathenson (1992); *PL*, Bonadonna and Houghton (2005); *WBL*, Bonadonna and Costa (2012)

trachyandesitic to trachydacitic (Fig. 2b; Table 3). Specifically, their major element compositions overlap partially with the proximal lapilli fall deposit from Marapi (MAR14-08), whilst their trace element compositions overlap significantly (Figs. 2b and 3; Table 3). In addition, the PCA and MEHCA analyses indicate Marapi as a likely source for AB2 and AB3 (Figs. 7 and 8). The radiocarbon median calibrated ages determined for AB2 and AB3 are 34,144 ± 184 and 35,673 ± 214 cal a BP (1σ; Table S10), respectively. A minimum volume of ~ 0.1 and ~ 0.6 km^3 was estimated for AB2 and AB3, corresponding to VEI 4 eruptions, with the method of Legros (2000).

AB4 and AB5 occur as 2- and 6-cm-thick, vitric, fine-grained and white ash horizons within cores GeoB10025-4 and GeoB10010-2, respectively. Juvenile glass compositions for these ash beds are rhyolitic and can be clearly differentiated in terms of major and trace element contents (Figs. 2b and 3; Table 3). Although no robust geochemical correlation with proximal deposits from West Sumatra is identified, clear compositional overlaps are observed between AB4 and RAN from Sumatra and between AB5 and DJT from Jambi (Fig. S1). These geochemical correlations are further validated by PCA and MEHCA analyses (Figs. 7 and 8). Radiocarbon median calibrated ages established for AB4 and AB5 are 36,761 ± 286 and 41,031 ± 283 cal a BP (1σ; Tables S10), respectively. Notably, the radiocarbon age obtained for AB4 is older than the proposed RAN eruption age of 34,012 ± 178 cal a BP (1σ; Natawidjaja et al. 2017; Table S9). However, we note that Natawidjaja et al. (2017) excluded three of four dated samples due to modern carbon contamination and assumed the remaining sample was the least affected. Due to the uncertainties of these ages, we consider the radiocarbon age for AB4, a more reliable eruption age estimate for the RAN. A minimum volume of ~ 4.0 and 7.3 km^3 was obtained for AB4 and AB5, equivalent to VEI 5 eruptions, using the method of Legros (2000).

AB6, AB7 and AB8 occur as 2-, 2.5- and 9-cm-thick, vitric, fine to coarse-grained and white ash horizons within cores GeoB10027-4, GeoB10027-4 and GeoB10025-4, respectively, from the northern Mentawai basin (Figs. 1 and 5; Table S2). Juvenile glass from ash beds AB6-AB8 are rhyolitic, but differences are discernible in both major and trace element contents (Figs. 2b and 3; Table 3). These ash beds do not correlate geochemically with any known proximal deposits. The radiocarbon median calibrated ages obtained for AB6, AB7 and AB8 are 41,614 ± 235, 39,048 ± 235 and 45,119 ± 518 cal a BP (1σ; Table S10), respectively.

AB9 is a 3-cm-thick, vitric, fine-grained and dark grey ash horizon, whereas AB10 is a vitric, fine-grained and black ash pod; both ash beds were sampled in core GeoB-10029–4 from the central Mentawai basin (Figs. 1 and 5; Table S2). Juvenile glass from AB9 and AB10 is trachydacitic (Fig. 2b; Table 3). Significantly, trace element glass compositions of AB9 demonstrate similarities to AB1 (i.e. low Ba/La, Rb/Y and La/Sm, as well as high La/Th ratios), whilst those from AB10 partially overlap with Tandikat (Fig. 3; Table 3). However, PCA and MEHCA analyses do not indicate any correlation with known proximal sources (Figs. 8 and 9). Age constraints are unavailable for these ash beds as radiocarbon dating of sampled foraminifera exceeded the limits of the method.

Discussion

Explosive eruptions from central Sumatra and regionally far-travelled eruptions

Malintang

Correlation between C1, V-4 and proximal LKT established Malintang volcano as the source of the youngest (~ 1.53 ka), moderately explosive VEI 5 eruption (~ 1.9–2.0 km^3) with

origins in central Sumatra during the late Holocene. Despite its relatively young age and substantial volume, the proximal footprint for this eruption is almost absent on the coastal plain downwind from Malintang. Pumices sampled in a riverbed south of Malintang (MLT20-01) provided further evidence for past explosive activity at the volcano. However, as no associated primary outcrops have been uncovered yet, our knowledge about this eruption is limited beyond its geochemical characteristics. Considering the dominant prevailing winds, which commonly transport volcanic ash to regions currently under-represented in the distal tephra record (e.g. northwest of Malintang), it is unsurprising that LKT is the only Malintang eruption identified.

Marapi

A comparison of proximal and distal tephra records yielded important information about explosive eruptions from the Marapi volcano. Specifically, our datasets indicated a correlation between a Marapi scoria fall deposit (MAR14-08) and V-3. Notably, we did not identify V-3 in any of our cores; however, the missing tephra record could be attributed to a discrepancy between the dispersal direction and the core locations (i.e. our selection of cores failed to capture the distal footprint). Salisbury et al. (2012) proposed Marapi as the source for V-3 and calculated a minimum volume of 0.6 km^3, equivalent to a VEI 4 eruption. The provenance of AB2 and AB3 (~ 34.1 and ~ 35.7 ka) were attributed to Marapi based on distinct geochemical and statistical correlations. Additionally, AB2 and AB3 are likely sourced from sub-Plinian to Plinian VEI 4 eruptions based on their minimum eruptive volumes (~ 0.1 and ~ 0.6 km^3). Significantly, the distal tephra record demonstrates that Marapi is not only capable of frequent small (VEI ≤ 2) eruptions as represented historically but also produced at least two VEI 4 eruptions in the past ~ 36 kyr.

Tandikat

Correlation between C2 and C3, V-5 and proximal TDK II and I established Tandikat volcano as the source of two widely dispersed, young (~ 4.36 and ~ 4.94 ka) and moderately explosive VEI 5 eruptions (~ 1.5–2.0 and ~ 3.7–5.3 km^3) originating from central Sumatra during the Holocene. Significantly, these eruptions are temporally proximate (only ~ 0.58 kyr apart), which raises important petrological questions about the pre-eruptive magmatic conditions that led to these explosive eruptions in quick succession. Additionally, the widespread nature, distinctive glass chemistry and well-defined ages of the TDK II and I highlight their potential as regional tephrochronological markers.

TDK I is a well-exposed pyroclastic deposit that is pervasive proximally and distally throughout central Sumatra. Field observations and TError quantification of ESP indicate TDK I is likely formed due to a single Plinian-type eruption with a WSW dispersal axis, which indicates an eruption during an easterly wind-dominated phase of the quasi-biennial oscillation (Baldwin et al. 2001) with a plume height of $25.9^{+1.9}_{-2.0}$ km and a maximum wind speed of $21.3^{+6.5}_{-6.1}$ m/s that is consistent with modern wind speeds above the tropopause in Sumatra during easterly wind phases (Kalnay et al. 1996). The moderately sorted units near the base of the proximal pyroclastic successions are interpreted as the result of a less stable plume that characterised the initial phase of vent opening (e.g. Sulpizio et al. 2010). The rare occurrence of TDK II proximally limits potential interpretations about its eruption processes. However, the analogous stratigraphic characteristics of TDK II and I deposits, coupled with the smaller median grain size of TDK II deposits, might indicate a TDK II eruption with lower plume height and wind speed, higher degree of fragmentation or a combination of these factors.

Ranau and Djudjun

AB4 and AB5 (~ 36.8 and ~ 41.0 ka) were correlated to the RAN in South Sumatra and the DJT in Jambi, respectively, and are likely distal limits for two of the most far-travelled eruptions in the distal tephra record (> 700 and > 400 km from respective sources). AB4 and AB5 are products of large VEI 5 eruptions based on their minimum eruptive volumes (~ 4.0 and 7.3 km^3). According to these estimates, the eruptive volume for the RAN is underestimated considering it is the product of a caldera-forming eruption, whilst the DJT represents one of the largest moderately explosive eruptions regionally over the last ~ 40 kyr.

Conclusions

This study presents a late Pleistocene-Holocene record of explosive volcanism from central Sumatra based on a combination of geochemical, geochronological and tephrochronological datasets associated with distal tephra layers collected from deep-sea cores, as well as proximal pyroclastic deposits sampled throughout Sumatra. This improved tephrochronological framework helps strengthen our knowledge of lesser-known, moderately explosive Sumatran eruptions, refine existing volcanic hazards assessments essential for the mitigation of future Sumatran volcanic activity and enhance the integration of terrestrial and marine paleoenvironmental

archives regionally. The key findings from this study are summarised as follows:

(1) Thirteen ash beds/layers were identified in the distal tephra record. Five were correlated to West Sumatra volcanoes including three VEI 5 eruptions within the last ~5 kyr and two VEI 4 eruptions related to Marapi volcano in the past ~36 kyr; two were correlated to eruptions originating from Jambi and South Sumatra; and the remaining six are tephra deposits with unknown source provenances.
(2) The ~1.53 ka LKT from Malintang volcano is the youngest VEI 5 eruption from central Sumatra. The almost complete absence of LKT in the proximal record demonstrates the challenges associated with the preservation and identification of volcanic deposits in the equatorial region and underscores the importance of distal tephra archives in reconstructing the eruptive histories of Sumatran volcanic centres.
(3) The ~4.36 and ~4.94 ka TDK II and I from Tandikat volcano are two temporally proximate VEI 5 eruptions (only ~580 yr apart). The pervasiveness, distinctive chemistry and well-constrained ages of TDK II and I, highlights their potential as regional tephrochronological markers.
(4) A quantification of the ESP for TDK I indicates a single Plinian-type eruption with a plume height of $25.9^{+1.9}_{-2.0}$ km a.s.l.; a maximum wind speed of $21.3^{+6.5}_{-6.1}$ m/s; a maximum MER of $1.8^{+0.5}_{-0.5} \times 10^8$ kg/s; a tephra volume between $3.7^{+0.8}_{-0.5}$ and $5.3^{+1.4}_{-1.1}$ km^3; and an eruption duration between 6^{+3}_{-2} and 9^{+3}_{-6} h
(5) The ~41 ka DJT was identified >400 km northwest of its source area and is likely associated with a large volume VEI 5 eruption. This represents the first evidence for late Pleistocene explosive activity in Jambi within the last ~40 kyr.

Supplementary Information The online version contains supplementary material available at https://doi.org/10.1007/s00445-025-01813-4.

Acknowledgements The authors are grateful to the core repositories of MARUM – Center for Marine Environmental Sciences, University of Bremen, Bremen, Germany and the Federal Institute for Geoscience and Natural Resources (BGR), Hannover, Germany for providing the sample material from the deep-sea cores used in this study. We kindly thank Hahjung Chin and Nur Fairuz Binte Razali for assisting in the preparation of the tephra and radiocarbon material, as well as Jeffrey Oalmann for providing technical support during laser ablation analyses. We also express our gratitude to Karen Fontijn and Natalia Pardo for their constructive comments and suggestions that resulted in a significantly improved manuscript.

Author contributions Marcus Phua: conceptualisation, investigation, visualisation, writing—original draft, writing—review and editing. Francesca Forni: conceptualisation, investigation, writing— original draft, writing—review and editing. Steffen Eisele: conceptualisation, investigation, visualisation, writing—original draft. Hamdi Rifai: resources, validation. Mahyar Mohtadi: resources, validation, writing—review and editing. Andreas Lückge: resources, validation, writing—review and editing. Caroline Bouvet de Maisonneuve: conceptualisation, investigation, funding acquisition, writing—review and editing.

Data Availability All datasets are available in the supplementary information.

Code availability Not applicable.

Declarations

Conflict of interest The authors declare no competing interests.

References

Alloway BV, Pribadi A, Westgate JA, Bird M, Fifield LK, Hogg A, Smith I (2004) Correspondence between glass-FT and ^{14}C ages of silicic pyroclastic flow deposits sourced from Maninjau caldera, west-central Sumatra. Earth Planet Sci Lett 227:121–133. https://doi.org/10.1016/j.epsl.2004.08.014

Baldwin MP, Gray LJ, Dunkerton TJ, Hamilton K, Haynes PH, Randel WJ, Holton JR, Alexander MJ, Hirota I, Horinouchi T, Jones DBA, Kinnersley JS, Marquardt C, Sato K, Takahashi M (2001) The quasi-biennial oscillation. Rev Geophys 39(2):179–229. https://doi.org/10.1029/1999RG000073

Bellier O, Bellon H, Sébrier M, Sutanto MRC (1999) K-Ar age of the Ranau Tuffs: implications for the Ranau caldera emplacement and slip partitioning in Sumatra (Indonesia). Tectonophysics 312:347–359. https://doi.org/10.1016/s0040-1951(99)00198-5

Biass S, Bonadonna C (2011) A quantitative uncertainty assessment of eruptive parameters derived from tephra deposits: the example of two large eruptions of Cotapaxi volcano, Ecuador. Bull Volcanol 73:73–90. https://doi.org/10.1007/s00445-010-0404-5

Biass S, Bagheri G, Aeberhard W, Bonadonna C (2014a) TError: towards a better quantification of the uncertainty propagated during the characterization of tephra deposits. Stat Volcanol 1:2. https://doi.org/10.5038/2163-338X.1.2

Biass S, Bagheri G, Bonadonna C (2015) A MATLAB implementation of the Carey and Sparks (1986) model. https://theghub.org/resources/3922. Accessed 15 March 2024.

Biass S, Bagheri G, Aeberhard W, Bonadonna C (2014b) TError v1.0. https://doi.org/10.5281/zenodo.3590702. Accessed 15 March 2024.

Bonadonna C, Costa A (2012) Estimating the volume of tephra deposits: a new simple strategy. Geology 40:415–418. https://doi.org/10.1130/g32769.1

Bonadonna C, Houghton BF (2005) Total grain-size distribution and volume of tephra-fall deposits. Bull Volcanol 67:441–456. https://doi.org/10.1007/s00445-004-0386-2

Bouvet de Maisonneuve C, Bergal-Kuvikas O (2020) Timing, magnitude and geochemistry of major Southeast Asian volcanic eruptions: identifying tephrochronologic markers. J Quat Sci 35:272–287. https://doi.org/10.1002/jqs.3181

Bronk Ramsey C (2009) Bayesian analysis of radiocarbon dates. Radiocarbon 51(1):337–360. https://doi.org/10.1017/s0033822200033865

Brown SK, Crosweller HS, Sparks RSJ, Cottrell E, Deligne NI, Guerrero NO, Hobbs L, Kiyosugi K, Loughlin SL, Siebert L, Takarada S (2014) Characterisation of the quaternary eruption record: analysis of the large magnitude explosive volcanic eruptions (LaMEVE) database. J Appl Volcanol 3:5. https://doi.org/10.1186/2191-5040-3-5

Carey S, Sparks RSJ (1986) Quantitative models of the fallout and dispersal of tephra from volcanic eruption columns. Bull Volcanol 48:109–125. https://doi.org/10.1007/BF0104654

Chesner CA, Rose WI, Deino A, Drake R, Westgate JA (1991) Eruptive history of Earth's largest Quaternary caldera (Toba, Indonesia) clarified. Geology 19:200–203. https://doi.org/10.1130/0091-7613(1991)019%3c0200:ehoesl%3e2.3.co;2

Degruyter W, Bonadonna C (2012) Improving on mass flow rate estimates of volcanic eruptions. Geophys Res Lett 39:L16308. https://doi.org/10.1029/2012GL052566

Fierstein J, Nathenson M (1992) Another look at the calculation of fallout tephra volumes. Bull Volcanol 54:156–167. https://doi.org/10.1007/bf00278005

Forni F, Phua M, Bernard O, Fellin MG, Oalmann J, Maden C, Rifai H, Bouvet de Maisonneuve CB (2024) Remobilization and eruption of an upper crustal cumulate mush at the Singkut caldera (North Sumatra, Indonesia). J Volcanol Geotherm Res 445:107971. https://doi.org/10.1016/j.jvolgeores.2023.107971

U.S. Geological Survey (2018) Shuttle Radar Topography Mission (SRTM) 1 arc-second global dataset. U.S. Geological Survey, United States of America. https://doi.org/10.5066/F7PR7TFT

Heaton TJ, Köhler P, Butzin M, Bard E, Reimer RW, Austin WEN, Bronk Ramsey C, Grootes PM, Hughen KA, Kromer B, Reimer PJ, Adkins J, Burke A, Cook MS, Olsen J, Skinner LC (2020) Marine20 – the marine radiocarbon age calibration curve (0–55,000 cal BP). Radiocarbon 62(4):779–820. https://doi.org/10.1017/rdc.2020.68

Hebbeln D, Jennerjahn T, Mohtadi M, Andruleit H, Baumgart A, Birkicht M, Chiessi C, Damar A, Donner B, Fadly N, Gröning M, Hantoro WS, Hayn C, Kadarwati UR, Kamija K, Kepel TL, Krück N, Lamy F, Langer J, Mai HA, Mehring T, Meyer-Schack B, Mollenhauer G, Morisse O, Müller A, Permana AK, Pranowo WS, Ranawijaya DAS, Romero O, Ruhland G, Scholten J, Smit J, Spliethoff C, Steinke S, Thomas R, Wienberg C, Yurnaldi D (2006) Report and preliminary results of RV SONNE Cruise SO-184, PABESIA, Durban (South Africa) – Cilacap (Indonesia) – Darwin (Australia), July 8th - September 13th, 2005. Berichte aus dem Fachbereich Geowissenschaften der Universität Bremen, 246. Bremen, 142 pp. http://nbn-resolving.de/urn:nbn:de:gbv:46-ep000100431

Hendrasto M, Surono, Budianto A, Kristianto, Triastuty H, Haerani N, Basuki A, Suparman Y, Primulyana S, Prambada O, Loeqman A, Indrastuti N, Andreas AS, Rosadi U, Adi S, Iguchi M, Ohkura T, Nakada S, Yoshimoto M (2012) Evaluation of volcanic activity at Sinabung volcano, after more than 400 years of quiet. J Disaster Res 7(1):37–47. https://doi.org/10.20965/jdr.2012.p0037

Hogg AG, Heaton TJ, Hua Q, Palmer JG, Turney CSM, Southon J, Bayliss A, Blackwell PG, Boswijk G, Ramsey CB, Pearson C, Petchey F, Reimer P, Reimer R, Wacker L (2020) SHCal20 southern hemisphere calibration, 0–55,000 years cal BP. Radiocarbon 62(4):759–778. https://doi.org/10.1017/rdc.2020.59

Hosobuchi MN, Chigira M, Lim C, Komoo I (2021) Geological history controlling the debris avalanches of pyroclastic fall deposits induced by the 2009 Padang earthquake, Indonesia: the sequential influences of pumice fall, weathering, and slope undercut. Eng Geol 287:106104. https://doi.org/10.1016/j.enggeo.2021.106104

Hutchings SJ, Mooney WD (2021) The seismicity of Indonesia and tectonic implications. Geochem Geophys Geosyst 22(9):e2021GC009812. https://doi.org/10.1029/2021gc009812

Smithsonian Institution (2024) Global volcanism program. Smithsonian Institution, Washington, D.C., United States of America. http://www.volcano.si.edu/

Jochum KP, Willbold M, Raczek I, Stoll B, Herwig K (2005) Chemical characterisation of the USGS reference glasses GSA-1G, GSC-1G, GSD-1G, GSE-1G, BCR-2G, BHVO-2G and BIR-1G using EPMA, ID-TIMS. ID-ICP-MS and LA-ICP-MS Geostand Geoanalytical Res 29(3):285–302. https://doi.org/10.1111/j.1751-908X.2005.tb00901.x

Jochum KP, Stoll B, Herwig K, Willbold M, Hofmann AW, Amini M, Aarburg S, Abouchami W, Hellebrand E, Mocek B, Raczek I, Stracke A, Alard O, Bouman C, Becker S, Dücking M, Brätz H, Klemd R, De Bruin D, Canil D, Cornell D, De Hoog CJ, Dalpé C, Danyushevshy L, Eisenhauer A, Gao Y, Snow JE, Groschopf N, Günther D, Latkoczy C, Guillong M, Hauri EH, Höfer HE, Lahaye Y, Horz K, Jacob DE, Kasemann SA, Kent AJR, Ludwig T, Zack T, Mason PRD, Meixner A, Rosner M, Misawa K, Nash BP, Pfänder J, Premo WR, Sun WD, Tiepolo M, Vannucci R, Vennemann T, Wayne D, Woodhead JD (2006) MPI-DING reference glasses for in situ microanalysis: new reference values for element concentrations and isotope ratios. Geochem Geophys Geosyst 7(2):Q02008. https://doi.org/10.1029/2005GC001060

Kalnay E, Kanamitsu M, Kistler R, Collins W, Deaven D, Gandin L, Iredell M, Saha S, White G, Woollen J, Zhu Y, Chelliah M, Ebisuzaki W, Higgins W, Janowiak J, Mo KC, Ropelewski C, Wang J, Leetmaa A, Reynolds R, Jenne R, Dennis J (1996) The NCEP/NCAR 40-year reanalysis project. Bull Am Meteorol Soc 77(3):437–472. https://doi.org/10.1175/1520-0477(1996)077%3c0437:TNYRP%3e2.0.CO;2

Kuehn SC, Froese DG, Shane PAR, Intercomparison Participants INTAV (2011) The INTAV intercomparison of electron-beam microanalysis of glass by tephrochronology laboratories: results and recommendations. Quat Int 247(1–2):19–47. https://doi.org/10.1016/j.quaint.2011.08.022

Kutterolf S, Schindlbeck-Belo JC, Pank K, Schmitt AK, Wang L-Y, KL, (2023) The cenozoic marine tephra record in Indian Ocean deep drill sites. J Volcanol Geotherm Res 441:107875. https://doi.org/10.1016/j.jvolgeores.2023.107875

Lê S, Josse J, Husson F (2008) FactoMineR: an R package for multivariate analysis. J Stat Softw 25(1):1–18. https://doi.org/10.18637/jss.v025.i01

Le Maitre RW, Streckeisen A, Zanettin B, Le Bas MJ, Bonin B, Bateman P (2002) Igneous rocks: a classification and glossary of terms: recommendations of the international union of geological sciences subcommission on the systematics of igneous rocks. 2nd edition. Cambridge University Press, Cambridge. https://doi.org/10.1017/CBO9780511535581

Legros F (2000) Minimum volume of a tephra fallout deposit estimated from a single isopach. J Volcanol Geotherm Res 96(1–2):25–32. https://doi.org/10.1016/s0377-0273(99)00135-3

Lowe DJ, Pearce NJG, Jorgensen MA, Kuehn SC, Tyron CA, Hayward CL (2017) Correlating tephras and cryptotephras using glass compositional analyses and numerical and statistical methods: review and evaluation. Quat Sci Rev 175:1–44. https://doi.org/10.1016/j.quascirev.2017.08.003

Lucchi F (2013) Stratigraphy methodology for the geological mapping of volcanic areas: insights from the Aeolian archipelago (southern Italy). Geol Soc Lond Mem 37:37e53. https://doi.org/10.1144/M37.5

Mastin LG, Guffanti M, Servranckx R, Webley P, Barsotti S, Dean K, Durant A, Ewert JW, Neri A, Rose WI, Schneider D, Siebert L, Stunder B, Swanson G, Tupper A, Volentik A, Waythomas CF (2009) A multidisciplinary effort to assign realistic source parameters to models of volcanic ash-cloud transport and dispersion during eruptions. J Volcanol Geotherm Res 186:10–21. https://doi.org/10.1016/j.jvolgeores.2009.01.008

Natawidjaja DH, Bradley K, Daryono MR, Aribowo S, Herrin J (2017) Late quaternary eruption of the Ranau Caldera and new geological slip rates of the Sumatran Fault Zone in Southern Sumatra. Indonesia Geosci Lett 4:21. https://doi.org/10.1186/s40562-017-0087-2

Nathenson M, Fierstein J (2015) Spread sheet to calculate tephra volume for exponential thinning. Ghub. https://theghub.org/resources/3716

Newhall CG, Self S (1982) The volcanic explosivity index (VEI): an estimate of explosive magnitude for historical volcanism. J Geophys Res 87(C2):1231–1238. https://doi.org/10.1029/jc087ic02p01231

Ninkovich D (1979) Distribution, age and chemical composition of tephra layers in deep-sea sediments off western Indonesia. J Volcanol Geotherm Res 5(1–2):67–86. https://doi.org/10.1016/0377-0273(79)90033-7

Nurfiani D, Wang X, Gunawan H, Triastuty H, Hidayat D, Wei SJ, Taisne B, Bouvet de Maisonneuve C (2021) Combining petrology and seismology to unravel the plumbing system of a typical arc volcano: an example from Marapi, West Sumatra, Indonesia. Geochem Geophys Geosyst 22(4):e2020GC009524. https://doi.org/10.1029/2020gc009524

Paton C, Hellstrom J, Paul B, Woodhead J, Hergt J (2011) Iolite: freeware for the visualisation and processing of mass spectrometric data. J Anal at Spectrom 26(12):2508–2518. https://doi.org/10.1039/c1ja10172b

Phua M (2022) A quaternary record of explosive eruptions along the Western Sunda volcanic arc: insights into the eruptive histories of volcanoes in Sumatra, Indonesia. Doctoral thesis, Nanyang Technological University, Singapore. https://hdl.handle.net/10356/169640

Pribadi A, Mulyadi E, Pratomo I (2007) Mekanisme erupsi ignimbrit Kaldera Maninjau, Sumatera Barat. Indonesian J Geosci 2(1):31–41. https://doi.org/10.17014/ijog.2.1.31-41

Pyle DM (1989) The thickness, volume and grainsize of tephra fall deposits. Bull Volcanol 51:1–15. https://doi.org/10.1007/bf01086757

Salisbury MJ, Patton JR, Kent AJR, Goldfinger C, Djadjadiharadja Y, Hanifa U (2012) Deep-sea ash layers reveal evidence for large, late Pleistocene and Holocene explosive activity from Sumatra, Indonesia. J Volcanol Geotherm Res 231–232:61–71. https://doi.org/10.1016/j.jvolgeores.2012.03.007

Schmid R (1981) Descriptive nomenclature and classification of pyroclastic deposits and fragments: recommendations of the IUGS Subcommission on the Systematics of igneous rocks. Geol Rundsch 70:794–799. https://doi.org/10.1007/BF01822152

Southon J, Kashgarian M, Fontugne M, Metivier B, Yim WW-S (2002) Marine reservoir corrections for the Indian Ocean and Southeast Asia. Radiocarbon 44(1):167–180. https://doi.org/10.1017/s0033822200064778

Suhendro I (2024) Evidence of the weakly stratified crystalline magma feeding an explosive Plinian eruption: a case study of the Holocene 'Malalak Tephra' deposit Tandikat volcano, West Sumatra. Indonesia J Asian Earth Sci 262:106002. https://doi.org/10.1016/j.jseaes.2023.106002

Suhendro I, Toramaru A, Harijoko A, Wibowo HE (2022) The origins of transparent and non-transparent white pumice: a case study of the 52 ka Maninjau caldera-forming eruption. Indonesia J Volcanol Geotherm Res 431:107643. https://doi.org/10.1016/j.jvolgeores.2022.107643

Sulpizio R, Cioni R, Di Vito MA, Mele D, Bonasia R, Dellino P (2010) The Pomici di Avellino eruption of Somma-Vesuvius (3.9 ka BP). Part I: stratigraphy, compositional variability and eruptive dynamics. Bull Volcanol 72:539–558. https://doi.org/10.1007/s00445-009-0339-x

Szymanowski D, Forni F, Phua M, Jicha B, Lee DWJ, Hsu Y-J, Rifai H, Schoene B, Bouvet de Maisonneuve C (2023) A shifty Toba magma reservoir: improved eruption chronology and petrochronological evidence for lateral growth of a giant magma body. Earth Planet Sci Lett 622:118408. https://doi.org/10.1016/j.epsl.2023.118408

Vermeesch P (2018) IsoplotR: a free and open toolbox for geochronology. Geosci Front 9:1479–1493. https://doi.org/10.1016/j.gsf.2018.04.001

Whelley PL, Newhall CG, Bradley KE (2015) The frequency of explosive volcanic eruptions in Southeast Asia. Bull Volcanol 77:1–11. https://doi.org/10.1007/s00445-014-0893-8

Wiedicke-Hombach M, Ardhayastuti S, Bruns A, Delisle G, Goergens R, Hermawan T, Kanamatsu T, Lückge A, Mohtadi M, Mühr P, Rahadyan T, Riyadi A, Rühlemann C, Schippers A, Schlömer S, Taufik M, Teichert B, Vink A, Weiss W, Wijaya H, Wöhrl C, Zeibig M, Zoch D (2006) SO189–2, SUMATRA - das Kohlenwasserstoff-System des Forearc von Sumatra, Fahrtbericht BGR-Fahrt SO189 Leg 2 Geologie, Geochemie, Geomikrobiologie, Wärmestrom, RV Sonne, Jakarta, Indonesia (6.9.2006) - Jakarta, Indonesia (8.10.2006). Bundesanstalt für Geowissenschaften und Rohstoffe. Hannover. 213 pp. https://doi.org/10.2312/cr_so189_2

Wilson L, Walker G (1987) Explosive volcanic eruptions - VI. Ejecta dispersal in plinian eruptions: the control of eruption conditions and atmospheric properties. Geophys J Int 89(2):657–679. https://doi.org/10.1111/j.1365-246X.1987.tb05186.x

Woodhead JD, Hellstrom J, Hergt JM, Greig A, Maas R (2007) Isotopic and elemental imaging of geological materials by laser ablation inductively coupled plasma-mass spectrometry. Geostand Geoanalytical Res 31(4):331–343. https://doi.org/10.1111/j.1751-908X.2007.00104.x